電気学会論文誌 A（基礎・材料・共通部門誌）
IEEJ Transactions on Fundamentals and Materials
Vol.133 No.6 pp.362-365 DOI: 10.1541/ieejfms.133.362

Paper

Heat Control of Resonant Circuit using Ferrite-core for Hyperthermia Implant

Yoshinori Miyake* Non-member, Kazuya Kumagai* Non-member
Kazuhiko Watabe* Non-member, Tsutomu Yamada* Non-member
Tadakuni Sato** Non-member, Yasushi Takemura*a) Member

(Manuscript received Oct. 10, 2012, revised Feb. 13, 2013)

Resonant circuit is expected to be used as heating source for hyperthermia implants because it can be effectively heated by an applied AC magnetic field. It was previously reported that the size of the implant was successfully miniaturized down to 0.9 mm in diameter, which was less than the diameters of the 18G injection needle and catheter. However, after the implant is delivered in vivo, the temperature measurement of the implant is difficult. In order to realize a less-invasive treatment of cancer, the implant should have the capability to control its heating. The two types of resonant-circuit implants were prepared. A method to control the heating of the implant using a ferrite core is discussed in this paper.

Keywords : hyperthermia, resonant circuit, ferrite-core, temperature-sensitive ferrite

1. Introduction

Hyperthermia involves the thermal treatment of cancer utilizing the high thermal sensitivity of the cancer tissue relative to that of the normal tissue. The treatment heats the cancer tissue at over 42.5 °C to kill the cancer cells, whereas normal cells are hardly damaged at temperatures below 44 °C. This method has an advantage that there are few major side effects when compared with various established treatments such as surgical operation, chemotherapy, and radiotherapy. The heating method is classified into whole-body heating and local heating. Local heating aims to heat tumors located deep inside the body. The hyperthermia method using implants has been reported in terms of its ability to warm the tissues locally[1][2]. A resonant circuit, which is heated effectively by an external magnetic field, is one of the candidates for the implants[3][4].

Preliminary results on the temperature rise of resonant circuits heated by an external AC magnetic field have been reported[4][5]. To realize their delivery through an injection needle or a catheter into the human body, the miniaturization of the implant down to smaller than 1 mm is required. A smaller voltage is induced in an inductor coil of smaller diameter, thereby reducing temperature rise. In our previous experiments, the diameter of the resonant-circuit implants could be reduced to 0.9 mm with using a ferrite-core[6]. However, the temperature measurement of the resonant circuit delivered in vivo is difficult. The over-heating of implants must be avoided. Therefore, the implant should control its heating autonomously. In this study, a method to realize heat control is discussed.

2. Experiments

2.1 Moving the Ferrite Core Figure 1 (a) shows a resonant circuit consisting of a closed connection comprising an inductor and a capacitor. Figure 2 shows a photograph of the resonant-circuit implant using a core coil.

When an external AC magnetic field, H_{ext} is applied to the circuit, an electromotive force, v, is induced in the inductor. Figure 1 (b) shows the equivalent circuit under the applied AC magnetic field. The parameter r_s in the figure is a residual resistance, which is dominated by the resistance of the inductor. The residual

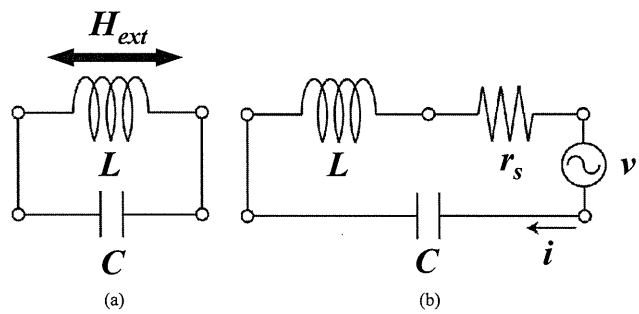

Fig. 1. Resonant circuit consisting of a closed connection of an inductor and a capacitor (a), and its equivalent circuit under an applied AC magnetic field (b)

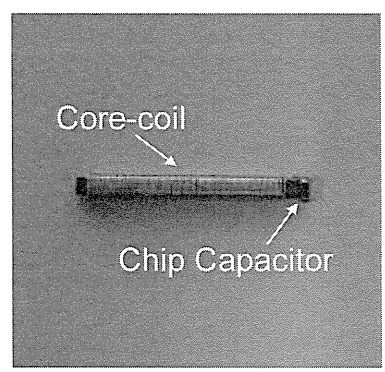

Fig. 2. Photograph of a resonant circuit using core-coil

a) Correspondence to: Yasushi Takemura. E-mail: takemura@ynu.ac.jp
* Graduate School of Engineering, Yokohama National University 79-5, Tokiwadai, Hodogaya-ku, Yokohama, Kanagawa 240-8501, Japan
** Graduate School of Biomedical Engineering, Tohoku University 6-6, Aoba, Aramaki, Aoba-ku, Sendai, Miyagi 980-8579, Japan

resistance is increased for an excitation at higher frequency. Electric power is consumed because of this residual resistance. The maximum consumed power P_{max} is obtained when the frequency of the applied field is equal to the resonant frequency of the circuit, f_r. P_{max} and f_r are described as Eqs. (1) and (2), respectively.

$$P_{max} = \frac{1}{r_s} v^2 \quad \cdots\cdots (1)$$

$$f_r = \frac{1}{2\pi\sqrt{LC}} \quad \cdots\cdots (2)$$

In Eq. (2), L is the inductance of coil and C is the capacitance of capacitor.

In order to deliver the implant of a resonant circuit into the body by a less-invasive method, e.g., via an injection needle or catheter, the size of the resonant-circuit implant should not exceed 1 mm. The size of the capacitor used in this study was as small as 0.7 mm, which was commercially distributed. The downsizing of the inductor causes the reduction of the induced voltage, thereby resulting in a lower power consumption by the resonant circuit. This is because the cross-section of the coil is reduced. The use of a ferrite core was examined in this study. By inserting the ferrite core into an inductor, the inductance and induced voltage increase.

Resonant circuit I consisted of a chip capacitor (1.0 μF) and a core coil having a variable inductance (1.5–2.7 μH) by changing the relative positions of the core and the coil, as shown in Fig. 3. Moving the core shifts the effective permeability in the coil, thereby shifting the inductance and resonant frequency of the circuit. The relationship between effective permeability and inductance is described as Eq. (3).

$$L = K\mu_0\mu_e\pi a^2 \frac{N^2}{l} \quad \cdots\cdots (3)$$

The parameters of the coil are: K the Nagaoka coefficient, μ_0 the permeability of free space, μ_e the relative permeability, a the radius, N the number of turns, l the length.

The inductor used in resonant circuit I was prepared by winding 40 turns of a 0.1-mm-thick copper wire around a NiCuZn spinel ferrite core (relative permeability at room temperature of 210, cross-section of 0.6 × 0.6 mm^2 and 5 mm in length). The specifications of resonant circuit I are summarized in Table 1. To confirm the resonant-frequency shift, the inductance and induced electromotive force of the inductor, and the temperature rise of the resonant circuit were measured by changing the position of the ferrite core. The inductance was evaluated using an impedance analyzer. Electromotive force was measured by applying an AC magnetic field of 1,500 A/m at frequency ranging from 20 to 200 kHz. The direction of the magnetic field was aligned such that it penetrated the inductor coil. Temperature rise was measured by applying an AC magnetic field of 1,500 A/m. The field frequency was varied near the resonant frequency of the circuit. Temperature was measured at 300 s after the application of the magnetic field by using an optical thermometer, whose sensor tip was attached to the inductor.

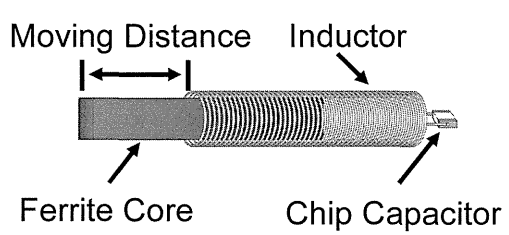

Fig. 3. Illustration of a resonant circuit with movable ferrite core

Table 1. Characteristics of resonant circuits

	I	II	III
Inductance [μH]	1.5-2.7	1.8	1.8
Capacitance [μF]	1.0	0.47	0.47
Curie temperature of ferrite core [°C]	330	55	60

2.2 Temperature-Sensitive Ferrite Core Resonant circuit II was consisted of a chip capacitor (0.47 μF) and a core-coil inductor (1.8 μH). The inductor was prepared with 40 turns of 0.1-mm-thick copper wire around a temperature-sensitive ferrite core (NiCuZn ferrite, relative permeability at room temperature of 1700, cross-section of 0.6 × 0.6 mm^2 and 5 mm in length). The Curie temperature of the core was 55 °C. The maximum temperature of the resonant circuit is expected to be limited by this Curie temperature as previously reported by Matsuki *et al.*[7][8]. Electromotive force was measured by applying an AC magnetic field of 200 A/m at frequency ranging from 20 to 200 kHz. Temperature rise of the resonant circuit was measured by applying an AC magnetic field from 500 to 3,000 A/m. The field frequency was 180 kHz. The other temperature-sensitive core of Curie temperature at 60 °C (NiCuZn ferrite, relative permeability at room temperature of 1600) was used for the inductor used in resonant circuit III. The specifications of resonant circuits II and III are summarized in Table 1.

3. Result and Discussion

3.1 Moving the Ferrite Core Figure 4 shows the inductance of the inductor used in resonant circuit I depending on the position of the ferrite core. The inductance decreased from 2.7 to 1.5 μH by changing the distance of the ferrite core from 0 to 2.5 mm. The distance is defined as indicated in Fig. 3.

Figure 5 shows the electromotive force induced in the inductor as a function of the position of the ferrite core. It was confirmed

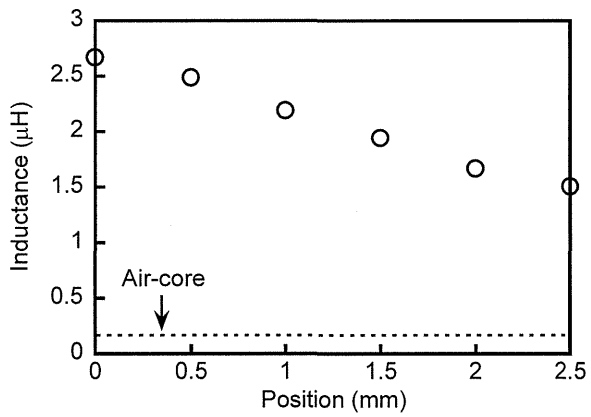

Fig. 4. Variation of the inductance of the inductor by changing the position of the ferrite core

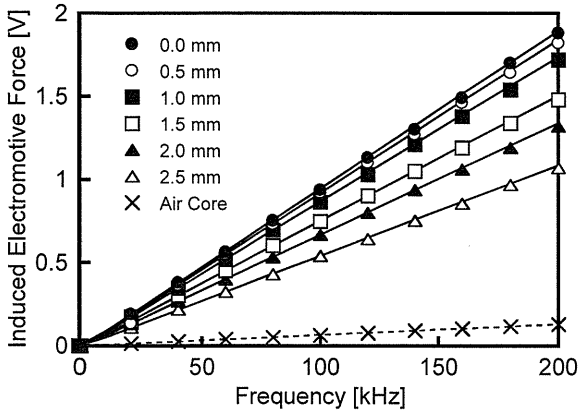

Fig. 5. Electromotive force induced in the inductor by changing the position of the ferrite core; The intensity of the applied AC magnetic field was 1,500 A/m

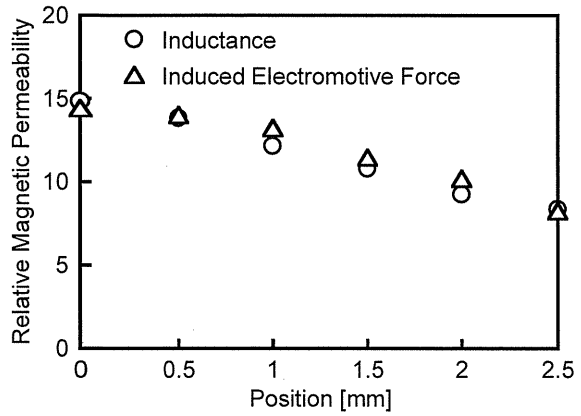

Fig. 6. Effective value of relative permeability of the inductor calculated from the measured inductance and electromotive force

that the effective permeability decreased by removing the ferrite core. The effective value of relative permeability was calculated from the measured inductance and electromotive force. They agreed well as shown in Fig. 6.

Figure 7 shows the frequency dependence of the temperature rise of the resonant-circuit implant. Temperature rise was measured 300 s after applying an AC magnetic field for the resonant circuit with various position of the core. It was confirmed that maximum temperature rise was obtained from the excitation frequency at the resonance. After the ferrite core was moved from 0 to 2.5 mm, resonant frequency was shifted from 130 to 200 kHz. With increasing the distance between the inductor and the core, the residual resistance was reduced slightly due to proximity effect. Moreover, the induced electromotive force is proportional to the frequency at fixed field intensity, thereby resulting in a higher temperature rise at higher frequency.

Figure 8 shows the resonant-frequency shift of the resonant circuit derived from the results of temperature rise and inductance. The result for temperature rise was generally in agreement with the value of the frequency shift calculated from the inductance in Eq. (2). The gap between the two results is presumably attributed to the temperature dependence of capacitance of a chip capacitor, which is slightly decreased by temperature.

3.2 Temperature Sensitive Ferrite Core Figure 9 shows the electromotive force induced in the inductors of resonant

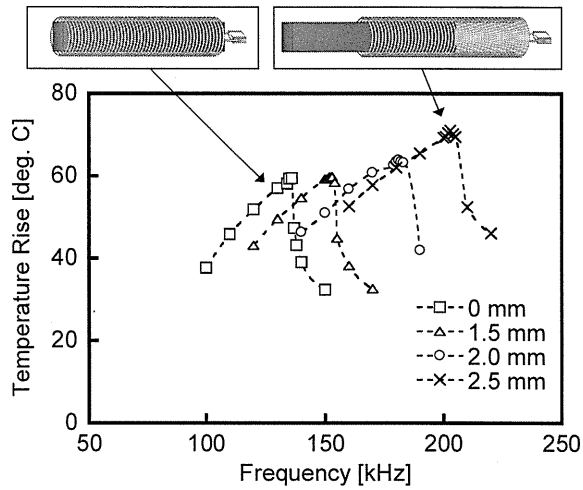

Fig. 7. Frequency dependence of the temperature rise of resonant circuit using the ferrite core measured 300 s after the application of an AC magnetic field while changing the position of the ferrite core; The field intensity was 1,500 A/m

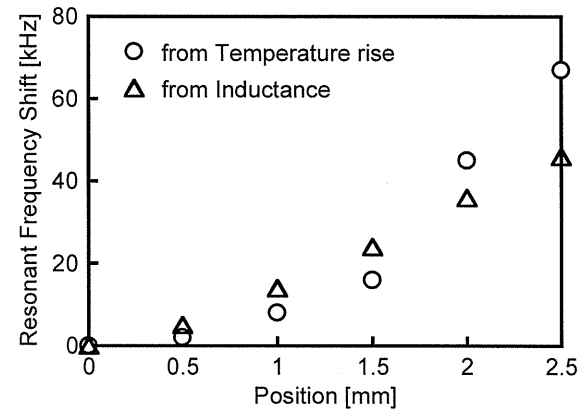

Fig. 8. Resonant-frequency shift of the resonant circuit derived from the results of temperature rise and inductance

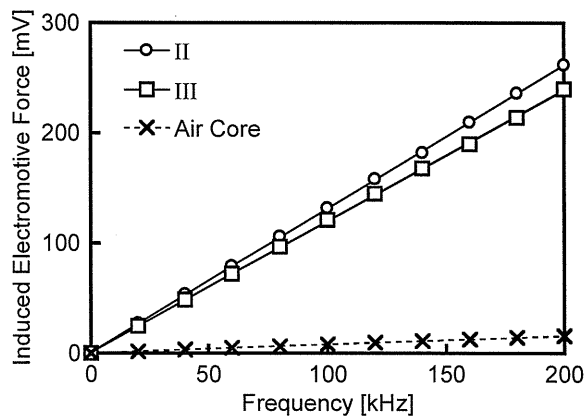

Fig. 9. Electromotive force induced in resonant circuits II and III; The applied AC magnetic field ranged from 20 to 200 kHz at 200 A/m

circuits II and III. The effective values of relative permeability of their inductors were 16.4 and 14.9. Figures 10 and 11 show the temperature rise of the resonant circuits II and III, respectively.

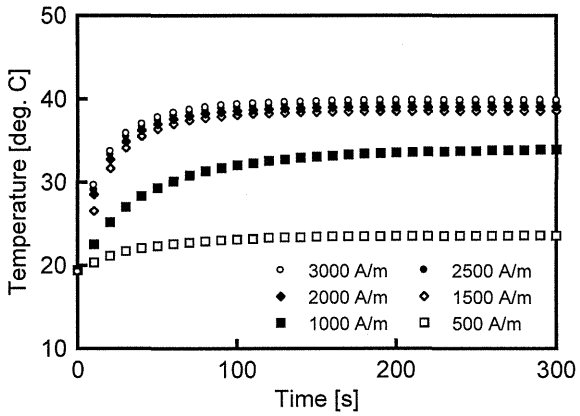

Fig. 10. Temperature rise of the resonant-circuit II; A temperature-sensitive ferrite core with its Curie temperature of 55 °C was used; The applied AC magnetic field was 180 kHz at various field intensities ranging from 500 A/m to 3,000 A/m

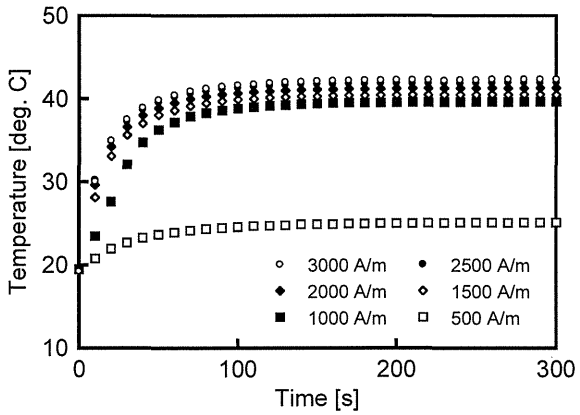

Fig. 11. Temperature rise of the resonant-circuit II; A temperature-sensitive ferrite core with its Curie temperature of 60 °C was used; The applied AC magnetic field was 180 kHz at various field intensities ranging from 500 to 3,000 A/m

When the field intensity was higher than 1,500 A/m, temperature rise was approximately constant. The temperature was almost saturated at 40 °C and 42 °C for resonant circuit II and III, while the Curie temperatures of temperature-sensitive ferrite core used in respective circuit were 55 °C and 60 °C, respectively. Because the sensor tip of the thermometer was attached to the outside surface of the inductor, the measured maximum temperature of the resonant circuit was lower than that of the Curie temperature of the temperature-sensitive ferrite core.

The temperature of the circuit was slightly increased even after it seemed to be limited by the Curie temperature of the core. It was because that the induced electromotive force in non-magnetic core was still increased with increasing the field intensity.

4. Conclusion

The temperature rise of the resonant-circuit implants was studied in order to realize a less-invasive treatment of cancer. The resonant circuit using the ferrite core exhibited a higher temperature rise relative to the resonant circuit using the air coil. Two methods for controlling the temperature of the resonant-circuit implant were studied. The resonant frequency was changed by varying the position of the coil core, resulting in control of the temperature rise. The temperature rise was also controlled by limiting at the Curie temperature of the ferrite core.

References

(1) I. Tohnai, Y. Goto, Y. Hayashi, M. Ueda, T. Kobayashi, and M. Matsui : "Preoperative thermochemotherapy of oral cancer using magnetic induction hyperthermia (implant heating system: HIS)", *Int. J. Hypertherm.*, Vol.12, pp.37-47 (1996)

(2) M. Jojo, A. Murakami, F. Sato, H. Matsuki, and T. Sato : "Consideration of handy excitation apparatus for the inductive hyperthermia", *IEEE Trans. Magn.*, Vol.37, No.4, pp.2944-2946 (2001)

(3) Y. Kotsuka, K. Orii, H. Kojima, K. Kamogawa, and M. Tanaka : "New wireless thermometer for RF and microwave thermal therapy using an MMIC in an Si BJT VCO type", *IEEE Trans. Microw. Theory Tech.*, Vol.47, No.12, pp.2630-2635 (1999)

(4) M. Morita, T. Inoue, T. Yamada, Y. Takemura, T. Niwa, and T. Inoue : "Resonant circuits for hyperthermia excited by RF magnetic field of MRI", *IEEE Trans. Magn.*, Vol.41, No.10, pp.3673-3675 (2005)

(5) T. Niwa, Y. Takemura, T. Inoue, H. Kurihara, and T. Hisa : "Implant hyperthermia resonant circuit produces heat in response to MRI unit radiofrequency pulses", *Brit. J. Radiol.*, Vol.81, pp.69-72 (2008)

(6) K. Watabe, K. Kumagai, R. Matsumura, T. Yamada, T. Sato, and Y. Takemura : "Hyperthermia implant consisting of resonant circuit delivered to tumor through 18 G needle", *IEEE Trans. Magn.*, Vol.47, No.10, pp.2887-2889 (2011)

(7) H. Matsuki, K. Murakami, and H. Niizuma : "Soft heating–A new method of heating using temperature-sensitive magnetic materials", *IEEE Trans. Magn.*, Vol.18, pp.1788-1790 (1982)

(8) H. Matsuki, F. Sato, Y. Sawaya, T. Maruyama, S. Aiba, Y. Ito, and T. Sato : "Mechanism of self control type hyperthermia based on advanced soft heating", *Jpn. J. Hyperthermic Oncol.*, Vol.22, No.3, pp.159-165 (2006)

Yoshinori Miyake (Non-member) is a master course student at Division of Electrical and Computer Engineering, Graduate School of Engineering, Yokohama National University, Japan.

Kazuya Kumagai (Non-member) is a master course student at Division of Electrical and Computer Engineering, Graduate School of Engineering, Yokohama National University, Japan.

Kazuhiko Watabe (Non-member) is a master course student at Division of Electrical and Computer Engineering, Graduate School of Engineering, Yokohama National University, Japan.

Tsutomu Yamada (Non-member) is a Research Associate at Division of Electrical and Computer Engineering, Yokohama National University, Japan.

Tadakuni Sato (Non-member) is a Researcher at Graduate School of Biomedical Engineering, Tohoku University, Japan.

Yasushi Takemura (Member) is a Professor at Division of Electrical and Computer Engineering, Yokohama National University, Japan.

frontiers in
INTEGRATIVE NEUROSCIENCE

ORIGINAL RESEARCH ARTICLE
published: 11 November 2013
doi:10.3389/fnint.2013.00076

In vivo evaluation of cellular activity in αCaMKII heterozygous knockout mice using manganese-enhanced magnetic resonance imaging (MEMRI)

Satoko Hattori[1,2,3], Hideo Hagihara[2,3], Koji Ohira[2,3], Ichio Aoki[4], Tsuneo Saga[4], Tetsuya Suhara[1], Makoto Higuchi[1]* and Tsuyoshi Miyakawa[2,3,5]*

[1] *Molecular Neuroimaging Program, Molecular Imaging Center, National Institute of Radiological Sciences, Chiba, Japan*
[2] *Division of Systems Medical Science, Institute for Comprehensive Medical Science, Fujita Health University, Toyoake, Aichi, Japan*
[3] *Japan Science and Technology Agency (JST), Core Research for Evolutional Science and Technology (CREST), Kawaguchi, Saitama, Japan*
[4] *Diagnostic Imaging Program, Molecular Imaging Center, National Institute of Radiological Sciences, Chiba, Japan*
[5] *Center for Genetic Analysis of Behavior, National Institute for Physiological Sciences, Okazaki, Aichi, Japan*

Edited by:
John J. Foxe, Albert Einstein College of Medicine, USA

Reviewed by:
Sebastian Cerdan, Instituto de Investigaciones Biomedicas Alberto Sols, Spain
Hadley Creighton Bergstrom, National Institutes of Health, USA

***Correspondence:**
Tsuyoshi Miyakawa, Division of Systems Medical Science, Institute for Comprehensive Medical Science, Fujita Health University, 1-98 Dengakugakubo Kutsukake-cho, Toyoake, Aichi 470-1192, Japan
e-mail: miyakawa@fujita-hu.ac.jp
Makoto Higuchi, Molecular Neuroimaging Program, Molecular Imaging Center, National Institute of Radiological Sciences, 4-9-1, Anagawa, Inage-ku, Chiba 263-8555, Japan
e-mail: mhiguchi@nirs.go.jp

The alpha-calcium/calmodulin-dependent protein kinase II (αCaMKII) is a serine/threonine protein kinase predominantly expressed in the forebrain, especially in the postsynaptic density, and plays a key role in synaptic plasticity, learning and memory. αCaMKII heterozygous knockout (HKO) mice exhibit abnormal emotional and aggressive behaviors and cognitive impairments and have been proposed as an animal model of psychiatric illness. Our previous studies have shown that the expression of immediate early genes (IEGs) after exposure to electric foot shock or after performing a working memory task is decreased in the hippocampus, central amygdala, and medial prefrontal cortex of mutant mice. These changes could be caused by disturbances in neuronal signal transduction; however, it is still unclear whether neuronal activity is reduced in these regions. In this study, we performed *in vivo* manganese-enhanced magnetic resonance imaging (MEMRI) to assess the regional cellular activity in the brains of αCaMKII HKO mice. The signal intensity of MEMRI 24 h after systemic $MnCl_2$ administration reflects functional increases of Mn^{2+} influx into neurons and glia via transport mechanisms, such as voltage-gated and/or ligand-gated Ca^{2+} channels. αCaMKII HKO mice demonstrated a low signal intensity of MEMRI in the dentate gyrus (DG), in which almost all neurons were at immature status at the molecular, morphological, and electrophysiological levels. In contrast, analysis of the signal intensity in these mutant mice revealed increased activity in the CA1 area of the hippocampus, a region crucial for cognitive function. The signal intensity was also increased in the bed nucleus of the stria terminalis (BNST), which is involved in anxiety. These changes in the mutant mice may be responsible for the observed dysregulated behaviors, such as cognitive deficit and abnormal anxiety-like behavior, which are similar to symptoms seen in human psychiatric disorders.

Keywords: αCaMKII, manganese-enhanced MRI, immature, dentate gyrus, hippocampus, bed nucleus of stria terminalis, schizophrenia, psychiatric disorder

INTRODUCTION

The alpha isoform of calcium/calmodulin-dependent protein kinase II (αCaMKII) is a calcium-activated, serine/threonine protein kinase and is abundant in the brain. It is enriched at the postsynaptic density (Lisman et al., 2002), and its activity is necessary for long-term potentiation of synaptic transmission in the hippocampus that may regulate learning and memory. Previous studies have shown that spatial learning and memory are affected in both homozygous and heterozygous αCaMKII knockout mice (Silva et al., 1992, 1996; Gordon et al., 1996; Frankland et al., 2001; Elgersma et al., 2002), as well as in several strains of αCaMKII transgenic mice (reviewed in Elgersma et al., 2004).

αCaMKII heterozygous knockout (HKO) mice also have various behavioral abnormalities that resemble symptoms seen in human psychiatric disorders, including decreased fear response, enhanced defensive aggression (Chen et al., 1994), increased locomotor activity, deficit in working memory, high level of social aggression toward cage mates, and an exaggerated infradian rhythm (Yamasaki et al., 2008). We found that molecular, morphological, and electrophysiological features in the dentate gyrus (DG) neurons of adult mutant mice were similar to those of immature DG neurons in normal rodents (Yamasaki et al., 2008). The "immature dentate gyrus (iDG)" phenotype has been observed in the post-mortem brains of patients with schizophrenia and bipolar disorder (Walton et al., 2012), as well as in other

mouse models of these disorders (Hagihara et al., 2011; Ohira et al., 2013; Takao et al., 2013). In addition, levels of dopamine D2 receptors in a state with a high affinity for dopamine ($D2^{High}$ receptors) were found to be elevated in the striatum of αCaMKII HKO mice, which could be representative of the hyperdopaminergic state seen in patients with schizophrenia (Novak and Seeman, 2010). Therefore, it has been proposed that αCaMKII HKO mice are promising animal models of schizophrenia and other psychiatric disorders (Yamasaki et al., 2008; Novak and Seeman, 2010) and that the iDG might serve as a novel endophenotype of the disorders, (Walton et al., 2012; Hagihara et al., 2013).

Our previous studies have shown that αCaMKII HKO mice had marked abnormalities in neurotransmitter binding to their receptors and neuronal activity in several brain regions (Yamasaki et al., 2008; Matsuo et al., 2009). Quantification of the expression of immediate-early genes (IEGs), which are activated in response to neuronal stimuli, exhibited lower expression levels of c-Fos in the DG, CA3, and central amygdaloid nucleus of the mutant mice than those of the wild-type mice following electric foot shock (Yamasaki et al., 2008). In the αCaMKII HKO mice, following a working memory version of the eight-arm radial maze task, the expressions of c-Fos were reduced in neurons of the hippocampal DG, CA1, and CA3 areas, central amygdala, and medial prefrontal cortex, whereas their expressions in the mutant mice kept in home cages were decreased in the DG, but not in other areas (Matsuo et al., 2009). In addition, the neurons in the mutant DG had abnormal electrophysiological features, including high excitability, small spike amplitude, and a decreased number of spikes during sustained depolarization (Yamasaki et al., 2008). These results suggest that αCaMKII HKO mice have functional deficits in several brain regions. However, it is possible that the altered expression of such IEGs is caused by a disruption in the signaling pathways that link neuronal activity to transcription, and it remains unclear whether neuronal activity is also altered in these regions of the mutant mice.

In this study, we evaluated the brains of αCaMKII HKO mice using systemically Mn^{2+} administrated MEMRI without blood-brain-barrier disruption (Watanabe et al., 2001; Aoki et al., 2004). This is an effective method to detect and visualize the anatomical and functional features of the brain. Mn^{2+} is a positive contrast agent for MRI and can accumulate in excitable cells via some of the transport mechanisms shared with calcium, such as voltage-gated Ca^{2+} channels and ionotropic glutamate receptors (Itoh et al., 2008; Silva and Bock, 2008; Hankir et al., 2012). The signal intensity on a T_1-weighted (T_1W) MR image is enhanced by Mn^{2+} uptake through activated ion channels; therefore, this technique can reflect the cellular activity in brain regions (Yu et al., 2005). We performed MRI scans on αCaMKII HKO and wild-type mice 1 day after systemic $MnCl_2$ intravenous administration, and assessed the normalized signal intensity under baseline conditions in the home cage.

MATERIALS AND METHODS

ANIMALS AND EXPERIMENTAL DESIGN

αCaMKII HKO mice generated by gene-targeting techniques were obtained from Jackson Laboratories (Bar Harbor, ME, USA). Mice were housed one per cage in a room with a 12 h light dark cycle (light on at 7:00 a.m.) with access to food and water *ad libitum*. MEMRI was performed on 7 to 10 month-old αCaMKII HKO mice ($n = 7$) and wild-type littermates ($n = 7$) on a C57BL/6J background. The Institutional Animal Care and Use Committee of the National Institute of Radiological Sciences and Fujita Health University approved the present experimental protocol.

MANGANESE ADMINISTRATION

Prior to the administration, 100 mM of $MnCl_2$ ($MnCl_2$-$4H_2O$, Sigma-Aldrich, St. Louis, MO, USA) was made with distilled water and diluted to 50 mM with saline to match the osmotic pressure of blood. We slowly infused 75 mg/kg (380 μmol/kg) $MnCl_2$ (total volume: 0.2–0.3 mL) for 60 min through the tail vein using a syringe pump (KDS-100, KD Scientific, Holliston, MA, USA). The $MnCl_2$ dose used in this study provided clear regional contrast and was similar to the doses used in previous MEMRI studies of the mouse brain (Yu et al., 2005; Lutkenhoff et al., 2012; Perez et al., 2013). After $MnCl_2$ injection, each mouse showed reduced locomotor activity temporarily for approximately 2–3 h, probably due to the toxic effect of $MnCl_2$. We did not notice any apparent differences in the behavioral response to $MnCl_2$ between genotypes. Mice were kept anesthetized with 0.5–1.5% isoflurane (Mylan Inc., Tokyo, Japan) during $MnCl_2$ infusion. Rectal temperature was continuously monitored and automatically maintained at approximately 37.5°C using a temperature controller (E5GN, Omron, Inc., Kyoto, Japan) and electrical heating pad (SG-15, Showa-Seiki industry, Inc., Kobe, Japan).

ANIMAL PREPARATION AND MRI MEASUREMENTS

We performed MRI in a 7.0 Tesla scanner, with a 40 cm bore magnet (Kobelco and Jastec, Tokyo, Japan) interfaced with a Bruker Avance-I console (BioSpec, Bruker Biospin, Ettlingen, Germany) with a volume coil for transmission (Bruker Biospin, Ettlingen, Germany) and a two-channel phased-array coil for reception (Rapid Biomedical, Rympar, Germany). Mice were anesthetized with 1.0–2.0% isoflurane and placed in prone position. During the experiment, a warm airflow over the animal was used to maintain its rectal temperature at 37.5°C. Respiratory rate was maintained at 20–40 breaths per minute and monitored throughout the experiment. Two-dimensional single-slice T_1W images were obtained by conventional spin-echo sequence with the following parameters: pulse repetition time (TR) = 250 ms; echo time (TE) = 9.574 ms; matrix size = 192 × 192; field of view = 1.92 × 1.92 cm^2; slice thickness = 1.0 mm; slice gap = 1 mm; spatial resolution = 100 × 100 × 1000 μm^3; and number of acquisitions = 4. A complete set of T_1W measurements consisted of two T_1W scans with slice offsets of 0 and 1 mm to maintain continuity of slices and to cover the entire brain. To register the image plane exactly, anatomical scout images were acquired using an incoherent, gradient-echo, fast low-angle shot sequence (TR = 100 ms; TE = 6 ms; matrix = 256 × 256; slice thickness = 2.0 mm). The slice orientation of the coronal plane was carefully adjusted on the sagittal scout image according to the landmarks of the pituitary body with reference to a mouse brain atlas (Paxinos and Franklin, 2001).

MRI DATA ANALYSIS

MR image data were converted from native Bruker format to voistat and TIFF files using PMOD (version 2.6; PMOD Technologies, Zurich, Switzerland), and analyzed quantitatively with PMOD and ImageJ.[1] Through comparison of MR images with a mouse brain atlas (Paxinos and Franklin, 2001), regions of interest (ROIs) for quantitative analysis of MEMRI were defined and delineated manually in the hippocampus, bed nucleus of the stria terminalis (BNST), cortex, striatum, thalamus, midbrain, and amygdala. We compared the MR image with the atlas based on the distance from the pituitary. Signal intensity was measured in each ROI, and we present the data normalized to that in the whole brain (Perez et al., 2013). In many cases, a slight signal intensity gradient was observed that could change within a plane and serve as noise. To minimize such noise, we used the average signal intensity of whole brain for normalization.

Statistical analyses were conducted using StatView software (SAS Institute, Cary, NC, USA). All data are presented as the mean ± the standard error of the mean (SEM), and were analyzed by one-way analysis of variance (ANOVA). An alpha level adjusted for multiple comparisons was calculated for each brain region by Bonferroni-Holm method.

QUANTIFICATION OF CELL NUMBER

Adult αCaMKII HKO mice ($n = 3$) and wild-type littermates ($n = 3$) were used. They were perfused through the heart with ice-cold phosphate buffered saline (PBS) and then with 4% paraformaldehyde (PFA) in 0.1 M PBS, with pH 7.4. After perfusion, the brains were immediately removed and immersed in the same fixative at 4°C overnight, followed by successive immersions in 30% sucrose in PBS. The brains were mounted in Tissue-Tek (Miles Inc., Elkhart, NY, USA), frozen, and stored at −80°C until use. Brains were sliced coronally into 10 μm thick sections on a cryostat (CM1850, Leica Microsystems, Wetzlar, Germany). The sections were stained with Hoechst 33258 (Polyscience, Warrington, PA, USA). Fluorescent signals were detected using a confocal laser-scanning microscope (LSM 700, Zeiss, Oberkochen, Germany). For the quantification of region size and Hoechst-stained cell numbers, we used ImageJ with the WCIF ImageJ bundle[2] (Takao et al., 2013). Three sections obtained from the anterior hippocampal region (from bregma −1.70 mm to bregma −2.30 mm, approximately) per animal were examined. ROI were delineated manually on the Hoechst-stained images with reference to the mouse brain atlas (Paxinos and Franklin, 2001). The values were then averaged within each brain and by group. All data collected in quantitative analyses were statistically evaluated using Student's t-test for comparison of means.

RESULTS

Normalized signal intensities of MEMRI responses in several anatomically defined ROIs were calculated semiquantitatively in αCaMKII HKO and wild-type mice. **Figure 1A** shows T_1W MR images of horizontal and coronal slices 1 day after $MnCl_2$ administration. The normalized signal intensity in MEMR images was significantly lower in the DG of mutant mice than in the DG of wild-type mice (**Figures 1A, B**, mutant vs. wild-type: 1.317 ± 0.007 vs. 1.397 ± 0.012, $F_{1,12} = 46.994$, $p < 0.0001$; adjusted $\alpha = 0.0063$). In contrast, the CA1 field including stratum radiatum, which is a projection area of the CA3, showed higher signal enhancement in αCaMKII HKO mice (**Figure 1A**). Normalized signal intensity was significantly higher in the CA1 of mutant mice than in the CA1 of wild-type mice (**Figure 1B**, mutant vs. wild-type: 1.215 ± 0.005 vs. 1.165 ± 0.005, $F_{1,12} = 71.086$, $p < 0.0001$; adjusted $\alpha = 0.0056$). However, there was no significant difference in normalized signal intensity in the CA3 region between the two genotypes (**Figure 1B**, mutant vs. wild-type: 0.937 ± 0.008 vs. 0.934 ± 0.016, $F_{1,12} = 0.041$, $p = 0.8438$). A scatter plot showing the relationship between normalized signal intensity in the DG and CA1 field (**Figure 1C**) indicates that the subregional profile of hippocampal cellular activity in the αCaMKII HKO mice is clearly distinct from that in the normal mice.

Signal intensity in MEMRI could reflect cell density in addition to cellular activity. The cell density in the mutant mice was assessed by Hoechst stain. In the DG, a significant increase in cell density was detected in the mutant mice (mutant vs. wild-type: 2357 ± 83 vs. 1578 ± 57, $p = 0.0012$) as compared to in the wild-type mice, which is likely the result of greatly increased adult neurogenesis in the DG of mutant mice (Yamasaki et al., 2008). There were no significant differences in cell density in the CA1 (mutant vs. wild-type: 1256 ± 8 vs. 1234 ± 45, $p = 0.2026$) and CA3 fields (mutant vs. wild-type: 552 ± 6 vs. 581 ± 18, $p = 0.4926$) between genotypes. In general, signal intensity in MEMRI is expected to be positively correlated with cell density (Silva et al., 2004), given that there is no difference in cellular activity. However, in the mutant mice, the signal intensity of the DG decreased, while cell density increased. These results suggest that decreased signal intensities in mutant mice are due to decreased cellular activity, not to increased cell density. Total cell numbers counted were 112.3 ± 11.9 in wild-type mice and 159.3 ± 2.9 in mutant mice in the dorsal part of the granule cell layer ($p = 0.0183$), 87.7 ± 7.5 in wild-type mice and 88.7 ± 3.2 in mutant mice in the pyramidal cell layer of CA1 ($p = 0.9084$), and 130.7 ± 7.5 in wild-type mice and 154.7 ± 6.6 in mutant mice in the pyramidal cell layer of CA3 ($p = 0.0742$).

In addition to the hippocampus, we observed increased MEMRI signal in the BNST of αCaMKII HKO mice (**Figure 2A**), and normalized signal intensity of the BNST was significantly higher in mutant mice than in wild-type mice (**Figure 2B**, mutant vs. wild-type: 1.024 ± 0.009 vs. 0.983 ± 0.012, $p = 0.0069$; adjusted $\alpha = 0.0071$). We also estimated normalized signal intensity in the major regions of the brain, such as the cortex, striatum, thalamus, midbrain, and amygdala. No significant differences were observed in the signal intensity of MEMRI in these regions between genotypes (**Figure 2C**, cortex: $F_{1,12} = 0.174$, $p = 0.6836$; striatum: $F_{1,12} = 0.090$, $p = 0.7691$; thalamus: $F_{1,12} = 0.005$, $p = 0.9442$; midbrain: $F_{1,12} = 1.390$, $p = 0.2613$; amygdala: $F_{1,12} = 0.127$, $p = 0.7273$). We also analyzed the data using signal intensities of the cortex or striatum for normalization, which yielded essentially the same results as those derived from the analysis using the signal intensities of the whole brain for normalization (data not shown).

[1] http://rsb.info.nih.gov/ij/download.html

[2] http://www.uhnresearch.ca/facilities/wcif/download.php

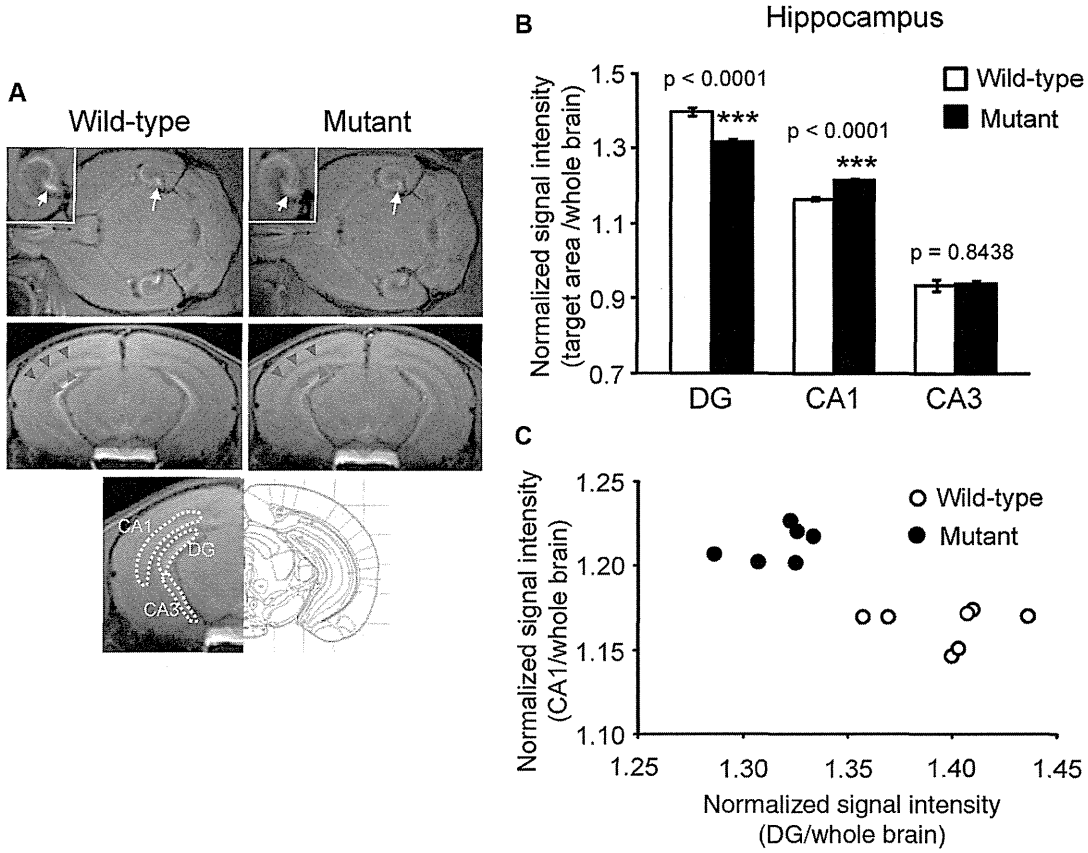

FIGURE 1 | Signal intensity decreased in the DG and increased in the CA1 region of αCaMKII HKO mice. (A) Representative T_1W MR images after systemic $MnCl_2$ administration. The top row shows horizontal slices at the level of the hippocampus. White squares indicate areas of the hippocampus presented at a high magnification. White arrows indicate the V-shaped structure of the DG. The middle row shows coronal slices including the hippocampal structure (bregma: −3.08 mm). The CA1 and stratum radiatum, including the projection area of the CA3, are indicated by red and blue arrowheads, respectively. The bottom row shows the anatomical location of ROIs in the hippocampus. The ROIs correspond to the DG, CA1, and CA3, respectively. **(B)** Normalized signal intensities in the hippocampal subregions are presented as the mean ± SEM. The *p* values indicate genotype effect in one-way ANOVA. **(C)** Scatterplot of normalized signal intensity in the DG versus CA1 region.

DISCUSSION

The αCaMKII HKO mouse has been proposed as an animal model of psychiatric illnesses, including schizophrenia and bipolar disorders. In this study, MEMRI demonstrated that Mn^{2+} accumulation was reduced in the DG and elevated in the BNST and CA1 field of the hippocampus.

We previously reported that αCaMKII HKO mice exhibited the iDG phenotype, a potential brain endophenotype shared by patients with schizophrenia and bipolar disorder (Walton et al., 2012; Hagihara et al., 2013; Shin et al., 2013). In the mutant DG, IEGs expression is abolished almost completely following a working memory task and electric foot shocks (Yamasaki et al., 2008; Matsuo et al., 2009), and electrophysiological evidence has revealed a decrease in the number of spikes during sustained depolarization (Yamasaki et al., 2008). These findings suggest that there is a decrease in neuronal activity and/or a disruption in the signal transduction pathway required to induce IEGs in the mutant DG. In this study, we examined the activity profile in the brains of mutant mice by performing MEMRI. A lower signal intensity of MEMRI was observed in the V-shaped structure of the DG in αCaMKII HKO mice than in that of the wild-type mice, and this might be the result of reduced activity in DG granule cells. Several lines of evidence support the reduction of activity in the DG. Downregulation in the expression levels of Ca^{2+}-permeable receptors could lead to the low activity observed in the DG of mutant mice. We have reported a decrease in N-methyl-D-aspartate (NMDA) receptor binding by using autoradiographic techniques (Yamasaki et al., 2008). Decreased Mn^{2+} influx through these receptors could be detected on the MEMRI as differences in Mn^{2+}-enhanced signal intensity in the granule cells of mutant mice. Alternatively, the activation of local circuits by immature neurons in the DG could inhibit the activity of the entire DG. Lacefield et al. proposed the possibility that immature granule cells effectively drive hilar interneurons, which innervate back to all granule cells (Lacefield et al., 2012). Thus, an excess of immature neurons may cause gross inhibition of the DG by

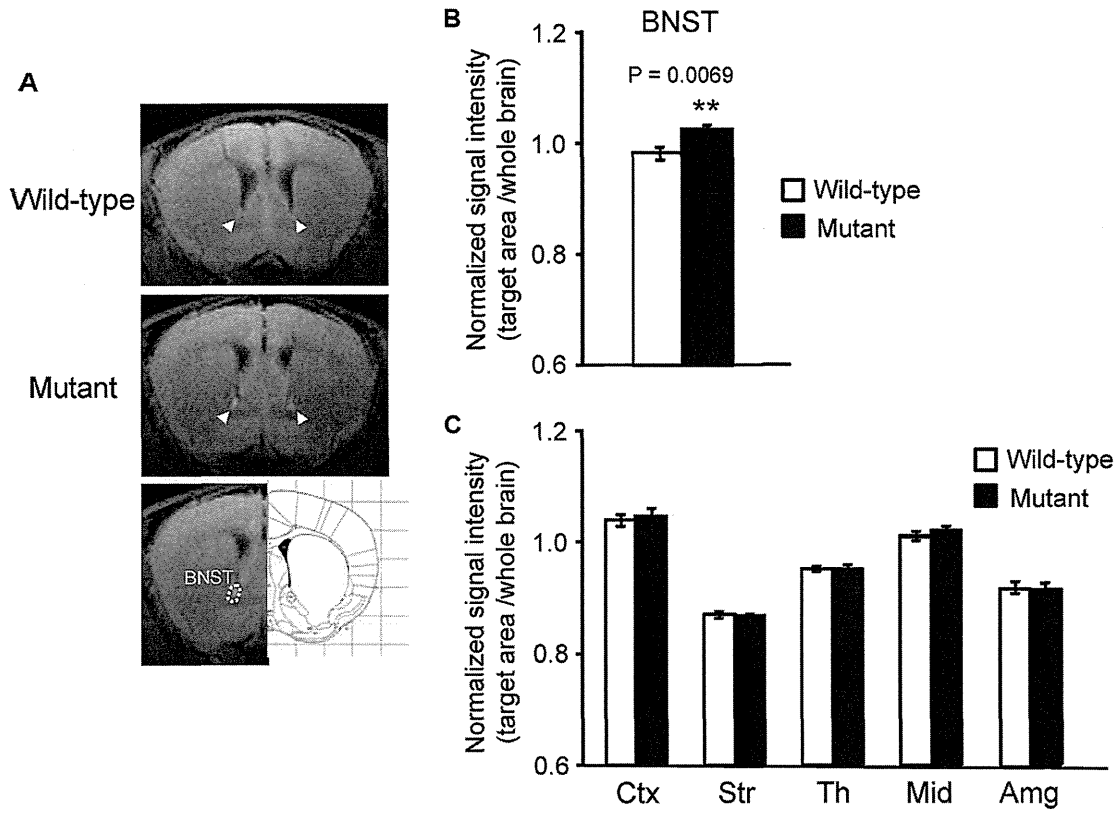

FIGURE 2 | Signal intensity increased in the BNST of αCaMKII HKO mice. **(A)** Representative T_1W MR images after systemic $MnCl_2$ administration. The top and middle rows show coronal slices at the level of the BNST (bregma: + 0.62 mm). The BNST is indicated by white arrowheads. The bottom row shows the anatomical location of ROIs in the BNST. **(B)** Normalized signal intensity in the BNST is presented as the mean ± SEM for the indicated numbers of animals **(C)** Normalized signal intensities in other regions of the brain are presented as the mean ± SEM.The *p* values indicate the effect of genotype in one-way ANOVA.

a feedback loop and result in the reduced enhancement of MRI signal intensity observed in the DG of mutant mice.

In contrast to the DG, the CA1 field of the αCaMKII HKO mice showed greater Mn^{2+} uptake, especially the stratum radiatum, which contains projection fibers to CA1 neurons. This result supports the idea of increased activity in the CA1 field of mutant mice. One possibility is that the augmentation in CA1 neuronal activity could be caused by an altered response to inputs from the entorhinal cortex (EC). The hippocampus mainly includes two excitatory networks, the monosynaptic pathway (from layer III in EC to CA1) and the trisynaptic pathway (from layer II in EC to DG to CA3 to CA1) (Amaral and Witter, 1989). Dysfunction in the mutant DG could reduce neuronal transmission in the trisynaptic pathway, and, therefore, homeostatic regulation of hippocampal network activity might lead to an increase in monosynaptic excitation of the CA1 region. Additionally, the decreased activity in the DG of these mice might cause activation in the CA3 and then in the CA1 field. Mossy fibers from the DG release the excitatory neurotransmitter glutamate (Henze et al., 2000). In the CA3, mossy fibers project to GABAergic interneurons that provide inhibitory inputs to CA3 pyramidal cells, and also terminate in CA3 pyramidal neurons (Henze et al., 2000). Activity of the DG and mossy fibers may result in a net inhibition within the CA3 network and presumably activate only a specific subset of CA3 pyramidal neurons (Henze et al., 2000; Song et al., 2012). In the αCaMKII HKO mice, decreased DG activity may lead to a tonic net activation of the CA3 and CA1 through a trisynaptic pathway. In this study, no difference in the MEMRI signal intensity ratio between genotypes could be detected in the CA3 area. This might result from limitations related to our methodology, including spatial resolution and detection sensitivity. Finally, the increased activity might be an effect of the HKO of αCaMKII itself in cells present in the CA1 area. Our previous study demonstrated a downregulation in serotonin 1A receptor binding and an upregulation of serotonin transporter binding in the CA1 of mutant mice (Yamasaki et al., 2008). Such abnormalities in the CA1 may have caused the increased activity. Further detailed studies, combined with *in vivo* imaging and electrophysiological methods, are needed to address the activity in each hippocampal subregion of the mutant mice.

A previous study revealed that the area showing enhanced signal on Mn^{2+}-contrasted MRI corresponds to the area that

exhibits increased expression of IEGs (Morita et al., 2002). In the DG, our result is consistent with this observation. However, there is a discrepancy between MEMRI signal intensity and c-Fos expression in the CA1. The expression of c-Fos following a working memory task was decreased in the mutant (Matsuo et al., 2009), and there was no significant difference in its expression in the CA1 of both genotypes after electrical foot shock and when the mice were kept in the home cage (Yamasaki et al., 2008; Matsuo et al., 2009). The inconsistency may be due to signal transduction abnormalities in IEG expression and/or to differences in experimental conditions, including the type of stimuli presented to the mice.

Additionally, previous studies suggested that the accumulation of reactive astrocytes and/or the migration of microglia could also cause increased signal intensity of MEMRI (Widerøe et al., 2009; Kawai et al., 2010). In αCaMKII HKO mice, the expression of glial fibrillary acidic protein, a well-established marker of astrocytes, is increased in the DG and CA1 area, especially the stratum radiatum and stratum oriens (unpublished data). In contrast, no significant difference between genotypes was observed in the immunoreactivity of ionized calcium binding adaptor molecule 1, a microglia/macrophage-specific calcium binding protein, in either the DG or CA1 field (unpublished data). These data suggest that decreased Mn^{2+} uptake in the mutant DG could be mainly due to altered neuronal activity. On the other hand, it is possible that the increased signal intensity of MEMRI, which was observed in the CA1 of mutant mice, was influenced by an increase in reactive astrocytes as well as by changes in neuronal activity.

In αCaMKII HKO mice, altered signal intensity in MEMRI was observed in the hippocampus, a region that plays a key role in cognitive functions such as working memory (Goldman-Rakic, 1994) and pattern separation (Gilbert et al., 2001; Gilbert and Kesner, 2003; Lee and Kesner, 2004a,b; Leutgeb et al., 2007; McHugh et al., 2007; Nakashiba et al., 2008). Impairments in hippocampal function are often observed in patients with psychiatric disorders such as schizophrenia and anxiety disorders (Goldman-Rakic, 1994) and may represent a behavioral endophenotype of these disorders. We demonstrated that αCaMKII HKO mice had severe deficits in working memory (Yamasaki et al., 2008), and that the density of c-Fos-positive cells in the hippocampus after a working memory task was significantly lower in the mutant mice than in the wild-type mice (Matsuo et al., 2009). In the EC of mutant mice, IEG expression was induced to the same extent as that observed in wild-type mice after the task. Thus, reduced or aberrant neuronal activity in the DG, which is a key input node for the hippocampal trisynaptic pathway, might lead to altered hippocampal network activity and impaired working memory performance in mutant mice. Indeed, previous studies have shown that rats with lesions of the DG are impaired in their ability to perform a working memory version of the eight-arm radial maze task (McLamb et al., 1988; Emerich and Walsh, 1989; Morris et al., 2012). It is possible that working memory dysfunction in mutant mice is caused by impaired rapid encoding of spatial information.

The mutant mice also showed increased MEMRI signal intensity in the BNST. This region has roles in the regulation of the hypothalamic-pituitary-adrenal axis response to acute stress (Choi et al., 2007). Recent studies in mice demonstrated that the oval nucleus increases anxiety-like behavior, while anterodorsal subregions of the BNST decrease anxiety-like behavior (Kim et al., 2013), and that BNST excitatory and inhibitory projections differentially produce anxiogenic and anxiolytic behavioral phenotypes, respectively (Jennings et al., 2013). These findings suggest that BNST acts as a crucial circuit node for bidirectional regulation of anxiety related responses. It is possible that increased BNST activity underlies decreased anxiety-like behavior in the αCaMKII mutant mice. During a casual visual inspection of the images, we noticed that the signal intensity was obviously increased in a discrete region of the BNST. There is a possibility that we could detect differences in signal intensities in other brain subregions as well. Future studies, using voxel-based analyses, are needed to assess the differences in detail.

In this study, we evaluated *in vivo* cellular activity in the brains of αCaMKII HKO mice by using MEMRI. It has been proposed that these mice are useful animal models of neuropsychiatric disorders (Yamasaki et al., 2008; Novak and Seeman, 2010; Hagihara et al., 2013; Shin et al., 2013). Our study is the first application of *in vivo* MEMRI in the mutant mice that focused on baseline activity rather than stimulus driven activity. Reduced excitatory signaling in the DG and increased activity in the CA1 appear to be associated with the pathological features of schizophrenia (Schobel et al., 2009; Tamminga et al., 2010). The results of the current study also suggest that cellular activity decreases in the DG and increases in the CA1 of mutant mice, providing additional support for the validity of these mice as an animal model of these disorders. The iDG and abnormal behavioral phenotypes are shared with Shn-2 knockout (Takao et al., 2013), mutant SNAP-25 knock-in (Ohira et al., 2013), and forebrain-specific calcineurin knockout mice (unpublished data). Chronic fluoxetine treatment and pilocarpine-induced seizures also lead to the iDG phenotype (Kobayashi et al., 2010; Shin et al., 2013). It is of interest to examine whether these mice show similar patterns of Mn^{2+} accumulation in MEMRI. Moreover, recent studies have demonstrated regional alteration of cellular activity in other animal models of neuropsychiatric disorders (Lutkenhoff et al., 2012; Perez et al., 2013). In addition to these studies, our results suggest that non-invasive MRI measurement is applicable for translational research of neuropsychiatric disorders. MEMRI of mutant mice would also provide biological outcome measures in screening of novel therapeutic compounds targeting these disorders.

ACKNOWLEDGMENTS

We thank Misao Yoneyama, Sayaka Shibata, and Takeo Shimomura for skillful assistance with the MR imaging experiments and Takeharu Minamihisamatsu for the maintenance and preparation of transgenic mice. This work was supported by grants from CREST of Japan Science and Technology Agency (JST), Grants-in-Aid for Japan Advanced Molecular Imaging Program and Scientific Research on Innovative Areas ("Brain Environment") from the Ministry of Education, Culture, Sports, Science and Technology, Japan, and partially by KAKENHI grant from the Japan Society for the Promotion of Science (JSPS).

REFERENCES

Amaral, D. G., and Witter, M. P. (2003). The three-dimensional organization of the hippocampal formation: a review of anatomical data. *Neuroscience* 31, 571–579. doi: 10.1016/0306-4522(89)90424-7

Aoki, I., Wu, Y.-J. L., Silva, A. C., Lynch, R. M., and Koretsky, A. P. (2004). In vivo detection of neuroarchitecture in the rodent brain using manganese-enhanced MRI. *Neuroimage* 22, 1046–1059. doi: 10.1016/j.neuroimage.2004.03.031

Chen, C., Rainnie, D. G., Greene, R. W., and Tonegawa, S. (1994). Abnormal fear response and aggressive behavior in mutant mice deficient for alpha-calcium-calmodulin kinase II. *Science* 266, 291–294. doi: 10.1126/science.7939668

Choi, D. C., Furay, A. R., Evanson, N. K., Ostrander, M. M., Ulrich-Lai, Y. M., and Herman, J. P. (2007). Bed nucleus of the stria terminalis subregions differentially regulate hypothalamic-pituitary-adrenal axis activity: implications for the integration of limbic inputs. *J. Neurosci.* 27, 2025–2034. doi: 10.1523/jneurosci.4301-06.2007

Elgersma, Y., Fedorov, N. B., Ikonen, S., Choi, E. S., Elgersma, M., Carvalho, O. M., et al. (2002). Inhibitory autophosphorylation of CaMKII controls PSD association, plasticity, and learning. *Neuron* 36, 493–505. doi: 10.1016/s0896-6273(02)01007-3

Elgersma, Y., Sweatt, J. D., and Giese, K. P. (2004). Mouse genetic approaches to investigating calcium/calmodulin-dependent protein kinase II function in plasticity and cognition. *J. Neurosci.* 24, 8410–8415. doi: 10.1523/jneurosci.3622-04.2004

Emerich, D. F., and Walsh, T. J. (1989). Selective working memory impairments following intradentate injection of colchicine: attenuation of the behavioral but not the neuropathological effects by gangliosides GM1 and AGF2. *Physiol. Behav.* 45, 93–101. doi: 10.1016/0031-9384(89)90170-4

Frankland, P. W., O'Brien, C., Ohno, M., Kirkwood, A., and Silva, A. J. (2001). Alpha-CaMKII-dependent plasticity in the cortex is required for permanent memory. *Nature* 411, 309–313. doi: 10.1038/35077089

Gilbert, P. E., and Kesner, R. P. (2003). Localization of function within the dorsal hippocampus: the role of the CA3 subregion in paired-associate learning. *Behav. Neurosci.* 117, 1385–1394. doi: 10.1037/0735-7044.117.6.1385

Gilbert, P. E., Kesner, R. P., and Lee, I. (2001). Dissociating hippocampal subregions: double dissociation between dentate gyrus and CA1. *Hippocampus* 11, 626–636. doi: 10.1002/hipo.1077

Goldman-Rakic, P. S. (1994). Working memory dysfunction in schizophrenia. *J. Neuropsych. Clin. Neurosci.* 6, 348–357.

Gordon, J. A., Cioffi, D., Silva, A. J., and Stryker, M. P. (1996). Deficient plasticity in the primary visual cortex of alpha-calcium/calmodulin-dependent protein kinase II mutant mice. *Neuron* 17, 491–499. doi: 10.1016/s0896-6273(00)80181-6

Hagihara, H., Graef, I. A., Crabtree, G. R., and Miyakawa, T. (2011). Forebrain-specific calcineurin deficiency causes immaturity of the dentate granule cells in adult mice. Sfn meeting 2001 abstract, Available at: http://ep65.eventpilotadmin.com/web/page.php?page=IntHtml&;project=SfN12&;id=33297.

Hagihara, H., Takao, K., Walton, N., Matsumoto, M., and Miyakawa, T. (2013). Immature dentate gyrus: an endophenotype of neuropsychiatric disorders. *Neural Plast.* 2013:318596. doi: 10.1155/2013/318596

Hankir, M. K., Parkinson, J. R., Bloom, S. R., and Bell, J. D. (2012). The effects of glutamate receptor agonists and antagonists on mouse hypothalamic and hippocampal neuronal activity shown through manganese enhanced MRI. *Neuroimage* 59, 968–978. doi: 10.1016/j.neuroimage.2011.08.063

Henze, D. A., Urban, N. N., and Barrionuevo, G. (2000). The multifarious hippocampal mossy fiber pathway: a review. *Neuroscience* 98, 407–427. doi: 10.1016/s0306-4522(00)00146-9

Itoh, K., Sakata, M., Watanabe, M., Aikawa, Y., and Fujii, H. (2008). The entry of manganese ions into the brain is accelerated by the activation of N-methyl-D-aspartate receptors. *Neuroscience* 154, 732–740. doi: 10.1016/j.neuroscience.2008.03.080

Jennings, J. H., Sparta, D. R., Stamatakis, A. M., Ung, R. L., Pleil, K. E., Kash, T. L., et al. (2013). Distinct extended amygdala circuits for divergent motivational states. *Nature* 496, 224–228. doi: 10.1038/nature12041

Kawai, Y., Aoki, I., Umeda, M., Higuchi, T., Kershaw, J., Higuchi, M., et al. (2010). In vivo visualization of reactive gliosis using manganese-enhanced magnetic resonance imaging. *Neuroimage* 49, 3122–3131. doi: 10.1016/j.neuroimage.2009.11.005

Kim, S.-Y., Adhikari, A., Lee, S. Y., Marshel, J. H., Kim, C. K., Mallory, C. S., et al. (2013). Diverging neural pathways assemble a behavioural state from separable features in anxiety. *Nature* 496, 219–223. doi: 10.1038/nature12018

Kobayashi, K., Ikeda, Y., Sakai, A., Yamasaki, N., Haneda, E., Miyakawa, T., et al. (2010). Reversal of hippocampal neuronal maturation by serotonergic antidepressants. *Proc. Natl. Acad. Sci. U S A* 107, 8434–8439. doi: 10.1073/pnas.0912690107

Lacefield, C. O., Itskov, V., Reardon, T., Hen, R., and Gordon, J. A. (2012). Effects of adult-generated granule cells on coordinated network activity in the dentate gyrus. *Hippocampus* 22, 106–116. doi: 10.1002/hipo.20860

Lee, I., and Kesner, R. P. (2004a). Differential contributions of dorsal hippocampal subregions to memory acquisition and retrieval in contextual fear-conditioning. *Hippocampus* 14, 301–310. doi: 10.1002/hipo.10177

Lee, I., and Kesner, R. P. (2004b). Encoding versus retrieval of spatial memory: double dissociation between the dentate gyrus and the perforant path inputs into CA3 in the dorsal hippocampus. *Hippocampus* 14, 66–76. doi: 10.1002/hipo.10167

Leutgeb, J. K., Leutgeb, S., Moser, M.-B., and Moser, E. I. (2007). Pattern separation in the dentate gyrus and CA3 of the hippocampus. *Science* 315, 961–966. doi: 10.1126/science.1135801

Lisman, J., Schulman, H., and Cline, H. (2002). The molecular basis of CaMKII function in synaptic and behavioural memory. *Nat. Rev. Neurosci.* 3, 175–190. doi: 10.1038/nrn753

Lutkenhoff, E., Karlsgodt, K. H., Gutman, B., Stein, J. L., Thompson, P. M., Cannon, T. D., et al. (2012). Structural and functional neuroimaging phenotypes in dysbindin mutant mice. *Neuroimage* 62, 120–129. doi: 10.1016/j.neuroimage.2012.05.008

Matsuo, N., Yamasaki, N., Ohira, K., Takao, K., Toyama, K., Eguchi, M., et al. (2009). Neural activity changes underlying the working memory deficit in alpha-CaMKII heterozygous knockout mice. *Front. Behav. Neurosci.* 3:20. doi: 10.3389/neuro.08.020.2009

McHugh, T. J., Jones, M. W., Quinn, J. J., Balthasar, N., Coppari, R., Elmquist, J. K., et al. (2007). Dentate gyrus NMDA receptors mediate rapid pattern separation in the hippocampal network. *Science* 317, 94–99. doi: 10.1126/science.1140263

McLamb, R. L., Mundy, W. R., and Tilson, H. A. (1988). Intradentate colchicine disrupts the acquisition and performance of a working memory task in the radial arm maze. *Neurotoxicology* 9, 521–528.

Morita, H., Ogino, T., Seo, Y., Fujiki, N., Tanaka, K., Takamata, A., et al. (2002). Detection of hypothalamic activation by manganese ion contrasted T(1)-weighted magnetic resonance imaging in rats. *Neurosci. Lett.* 326, 101–104. doi: 10.1016/s0304-3940(02)00330-0

Morris, A. M., Churchwell, J. C., Kesner, R. P., and Gilbert, P. E. (2012). Selective lesions of the dentate gyrus produce disruptions in place learning for adjacent spatial locations. *Neurobiol. Learn. Mem.* 97, 326–331. doi: 10.1016/j.nlm.2012.02.005

Nakashiba, T., Young, J. Z., McHugh, T. J., Buhl, D. L., and Tonegawa, S. (2008). Transgenic inhibition of synaptic transmission reveals role of CA3 output in hippocampal learning. *Science* 319, 1260–1264. doi: 10.1126/science.1151120

Novak, G., and Seeman, P. (2010). Hyperactive mice show elevated D2(High) receptors, a model for schizophrenia: calcium/calmodulin-dependent kinase II alpha knockouts. *Synapse* 64, 794–800. doi: 10.1002/syn.20786

Ohira, K., Kobayashi, K., Toyama, K., Nakamura, H. K., Shoji, H., Takao, K., et al. (2013). Synaptosomal-associated protein 25 mutation induces immaturity of the dentate granule cells of adult mice. *Mol. Brain* 6:12. doi: 10.1186/1756-6606-6-12

Paxinos, D. G., and Franklin, K. B. J. (2001). *The Mouse Brain in Stereotaxic Coordinates: Compact.* 2nd Edn. San Diego, California, USA: Academic Press.

Perez, P. D., Hall, G., Kimura, T., Ren, Y., Bailey, R. M., Lewis, J., et al. (2013). In vivo functional brain mapping in a conditional mouse model of human tauopathy (tau(P301L)) reveals reduced neural activity in memory formation structures. *Mol. Neurodegener.* 8:9. doi: 10.1186/1750-1326-8-9

Schobel, S. A., Lewandowski, N. M., Corcoran, C. M., Moore, H., Brown, T., Malaspina, D., et al. (2009). Differential targeting of the CA1 subfield of the hippocampal formation by schizophrenia and related psychotic disorders. *Arch. Gen. Psychiat.* 66, 938–946. doi: 10.1001/archgenpsychiatry.2009.115

Shin, R., Kobayashi, K., Hagihara, H., Kogan, J. H., Miyake, S., Tajinda, K., et al. (2013). The immature dentate gyrus represents a shared phenotype of mouse models of epilepsy and psychiatric disease. *Bipolar Disord.* doi: 10.1111/bdi.12064. [Epub ahead of print].

Silva, A. C., and Bock, N. A. (2008). Manganese-enhanced MRI: an exceptional tool in translational neuroimaging. *Schizophr. Bull.* 34, 595–604. doi: 10.1093/schbul/sbn056

Silva, A. C., Lee, J. H., Aoki, I., and Koretsky, A. P. (2004). Manganese-enhanced magnetic resonance imaging (MEMRI): methodological and practical considerations. *NMR Biomed.* 17, 532–543. doi: 10.1002/nbm.945

Silva, A. J., Paylor, R., Wehner, J. M., and Tonegawa, S. (1992). Impaired spatial learning in alpha-calcium-calmodulin kinase II mutant mice. *Science* 257, 206–211. doi: 10.1126/science.1321493

Silva, A. J., Rosahl, T. W., Chapman, P. F., Marowitz, Z., Friedman, E., Frankland, P. W., et al. (1996). Impaired learning in mice with abnormal short-lived plasticity. *Curr. Biol.* 6, 1509–1518. doi: 10.1016/s0960-9822(96)00756-7

Song, J., Christian, K. M., Ming, G., and Song, H. (2012). Modification of hippocampal circuitry by adult neurogenesis. *Dev. Neurobiol.* 72, 1032–1043. doi: 10.1002/dneu.22014

Takao, K., Kobayashi, K., Hagihara, H., Ohira, K., Shoji, H., Hattori, S., et al. (2013). Deficiency of schnurri-2, an MHC enhancer binding protein, induces mild chronic inflammation in the brain and confers molecular, neuronal, and behavioral phenotypes related to schizophrenia. *Neuropsychopharmacology* 38, 1409–1425. doi: 10.1038/npp.2013.38

Tamminga, C. A., Stan, A. D., and Wagner, A. D. (2010). The hippocampal formation in schizophrenia. *Am. J. Psychiat.* 167, 1178–1193. doi: 10.1176/appi.ajp.2010.09081187

Walton, N. M., Zhou, Y., Kogan, J. H., Shin, R., Webster, M., Gross, A. K., et al. (2012). Detection of an immature dentate gyrus feature in human schizophrenia/bipolar patients. *Transl. Psychiat.* 2:e135. doi: 10.1038/tp.2012.56

Watanabe, T., Michaelis, T., and Frahm, J. (2001). Mapping of retinal projections in the living rat using high-resolution 3D gradient-echo MRI with Mn2+-induced contrast. *Magn. Reson. Med.* 46, 424–429. doi: 10.1002/mrm.1209

Widerøe, M., Olsen, Ø., Pedersen, T. B., Goa, P. E., Kavelaars, A., Heijnen, C., et al. (2009). Manganese-enhanced magnetic resonance imaging of hypoxic-ischemic brain injury in the neonatal rat. *Neuroimage* 45, 880–890. doi: 10.1016/j.neuroimage.2008.12.007

Yamasaki, N., Maekawa, M., Kobayashi, K., Kajii, Y., Maeda, J., Soma, M., et al. (2008). Alpha-CaMKII deficiency causes immature dentate gyrus, a novel candidate endophenotype of psychiatric disorders. *Mol. Brain* 1:6. doi: 10.1186/1756-6606-1-6

Yassa, M. A., Hazlett, R. L., Stark, C. E. L., and Hoehn-Saric, R. (2012). Functional MRI of the amygdala and bed nucleus of the stria terminalis during conditions of uncertainty in generalized anxiety disorder. *J. Psychiatr. Res.* 46, 1045–1052. doi: 10.1016/j.jpsychires.2012.04.013

Yu, X., Wadghiri, Y. Z., Sanes, D. H., and Turnbull, D. H. (2005). In vivo auditory brain mapping in mice with Mn-enhanced MRI. *Nat. Neurosci.* 8, 961–968. doi: 10.1038/nn1477

Conflict of Interest Statement: Tsuyoshi Miyakawa is an advisor/consultant for Astellas Pharma Inc. The other authors declare that the research was conducted in the absence of any commercial or financial relationships that could be construed as a potential conflict of interest.

Received: 27 August 2013; accepted: 16 October 2013; published online: 11 November 2013.

Citation: Hattori S, Hagihara H, Ohira K, Aoki I, Saga T, Suhara T, Higuchi M and Miyakawa T (2013) In vivo evaluation of cellular activity in αCaMKII heterozygous knockout mice using manganese-enhanced magnetic resonance imaging (MEMRI). Front. Integr. Neurosci. 7:76. doi: 10.3389/fnint.2013.00076

This article was submitted to the journal Frontiers in Integrative Neuroscience.

JOURNAL OF MAGNETIC RESONANCE IMAGING 39:1550–1557 (2014)

Original Research

Neurochemistry in Shiverer Mouse Depicted on MR Spectroscopy

Jun-ichi Takanashi, MD, PhD,[1,2,3]* Nobuhiro Nitta, ME,[1] Nobuaki Iwasaki, MD, PhD,[4] Shigeyoshi Saito, PhD,[5] Ryuta Tanaka, MD, PhD,[6] A. James Barkovich, MD, PhD,[7] and Ichio Aoki, PhD[1]

Purpose: To evaluate the neurochemical changes associated with hypomyelination, especially to clarify whether increased total *N*-acetylaspartate (tNAA) with decreased choline (Cho) observed in the thalamus of *msd* mice with the *plp1* mutation is a common finding for hypomyelinating disorders.

Materials and Methods: We performed magnetic resonance imaging (MRI) and proton MR spectroscopy (^{1}H-MRS) of the thalamus and cortex of postnatal 12-week shiverer mice devoid of myelin basic protein (mbp), heterozygous and wild-type mice with a 7.0T magnet. Luxol Fast Blue staining and immunohistochemical analysis with anti-Mbp, Gfap, Olig2, and NeuN antibodies were also performed.

Results: In the thalamus, decreased Cho and normal tNAA were observed in shiverer mice. In the cortex, tNAA, Cho, and glutamate were decreased in shiverer mice. Histological and immunohistochemical analysis of shiverer mice brains revealed hypomyelination in the thalamus, white matter, and cortex; astrogliosis and an increased number of total oligodendrocytes in the white matter; and a decreased number of neurons in the cortex.

Conclusion: The reduction of Cho on ^{1}H-MRS might be a common marker for hypomyelinating disorders. A normal tNAA level in the thalamus of shiverer mice might be explained by the presence of mature oligodendrocytes, which enable neuron-to-oligodendrocyte NAA transport or NAA catabolism.

Key Words: magnetic resonance spectroscopy; *N*-acetylaspartate; choline; hypomyelination; myelin basic protein; shiverer mouse

J. Magn. Reson. Imaging 2014;39:1550–1557.

THE TERM HYPOMYELINATION describes a permanent, substantial deficit of myelin deposition in the brain. The protein composition of myelin in the central nervous system (CNS) is simpler than that of other membranes; the two major components are proteolipid protein (PLP) and myelin basic protein (MBP), which account for 50% and 30% of the total myelin protein, respectively. MBP, the second major structural protein of the myelin sheath of the mammalian CNS, is associated with the major dense line (1). Shiverer (*shi/shi*) is an autosomal recessive mouse mutation of the *mbp* gene, which deletes a 20-kb region including exons 3–7, resulting in the absence of mbp (1–3). Oligodendrocytes of shiverer mice fail to assemble compacted myelin (1,2), which causes an almost total lack of myelin (hypomyelination) in the CNS.

Despite progress in understanding the molecular basis and neuroimaging characteristics of Pelizaeus-Merzbacher disease (PMD) (4,5), a representative hypomyelination disease due to derangement of the *PLP1* gene, the neurochemical changes associated with hypomyelination remains unknown. We performed proton magnetic resonance spectroscopy (^{1}H-MRS) with a 7.0T magnet on the brains of *myelin synthesis-deficient* (*msd*) mice, a model of connatal PMD, one of the most severely affected murine mutants as to the *plp1* gene. ^{1}H-MRS of *msd* mice showed increased total *N*-acetylaspartate (tNAA; NAA, 2.01 ppm, and *N*-acetylaspartylglutamate [NAAG] 2.04 ppm, which are difficult to distinguish on ^{1}H-MRS) and decreased choline (Cho) (6), as observed in

[1]Molecular Imaging Center, National Institute of Radiological Sciences, Chiba, Japan.
[2]Department of Pediatrics, Kameda Medical Center, Kamogawa, Japan.
[3]Department of Radiology, Toho University Sakura Medical Center, Sakura, Japan.
[4]Department of Pediatrics, Ibaraki Prefectural University of Health Sciences, Amimachi, Japan.
[5]Department of Medical Physics and Engineering, Graduate School of Medicine, Osaka University, Suita, Japan.
[6]Department of Pediatrics, University of Tsukuba, Tsukuba, Japan.
[7]Department of Radiology and Biomedical Imaging, University of California San Francisco, California, USA.

Contract grant sponsor: Ministry of Health, Labor and Welfare of Japan; Contract grant numbers: Grant-in-aid for the Research on Measures for Intractable Diseases (H24-Nanchi-Ippan-072), Research Grant for Nervous and Mental Disorders (24-7); Contract grant sponsor: Grant-in-Aid for Scientific Research (C), JSPS; Contract grant numbers: 17591104, 24591790; Contract grant sponsor: Funding Program for World-Leading Innovative R&D on Science and Technology (FIRST Program).

*Address reprint requests to: J.T., Department of Pediatrics, Kameda Medical Center, 929 Higashi-cho, Kamogawa-shi, Chiba 296–8602, Japan. E-mail: jtaka44@hotmail.co.jp

Received February 5, 2013; Accepted June 18, 2013.
DOI 10.1002/jmri.24306
View this article online at wileyonlinelibrary.com.

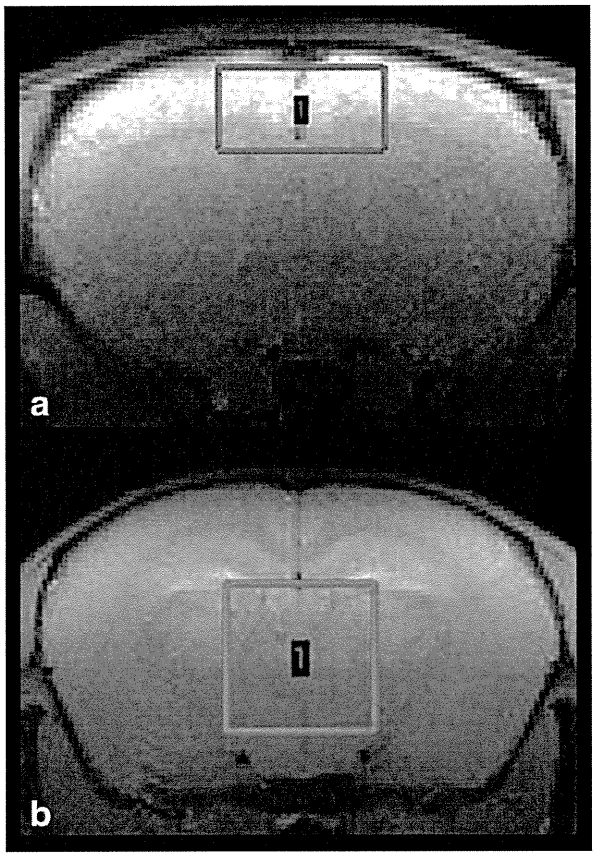

Figure 1. Coronal T1-weighted images show the ROI in the cortex (a) and thalamus (b) used for ^{1}H-MRS. [Color figure can be viewed in the online issue, which is available atwileyonlinelibrary.com.]

human PMD (7). Increased tNAA should attract attention because NAA is generally considered an important marker of neurons and axons (8,9), and is usually decreased in many neurodegenerative disorders. We performed ^{1}H-MRS in shiverer mice to determine the neurochemical changes associated with hypomyelination, especially to clarify whether or not increased tNAA with decreased Cho detectable on ^{1}H-MRS is a common finding for hypomyelinating disorders.

MATERIALS AND METHODS

Animals

The experimental animals included postnatal 12-week (12W) shiverer mice (*shi/shi*, maintained in the ICR background; $n=7$, 2 males and 5 females, weight = 32.5 ± 3.8 g), heterozygous mice (*shi/+*) ($n=8$, 3 males and 5 females, weight = 37.0 ± 6.1 g), and wild-type ICR mice ($n=8$, 4 males and 4 females, weight = 40.8 ± 7.3 g). Shiverer mice exhibit progressive tremors and tonic seizures early in life, which cause their premature death between 3 and 5 months of age. The animals had free access to food and water and were kept under standard laboratory conditions of 22–23°C room temperature, around 50% humidity, and a 12:12 hour light/dark cycle. Immediately prior to and during the MRI scanning, all mice were anesthetized with 2% isoflurane (Mylan Japan, Japan). The rectal temperature was continuously monitored and maintained at 36.5 ± 0.5°C using a heating pad throughout all experiments. During MRI scanning, the mice lay in the prone position on an MRI-compatible cradle and were held in place by a hand-made ear bar and anesthetized through a facemask with 2% isoflurane. The study protocols were approved by the Animal Welfare Committee of the National Institute of Radiological Sciences and that of the Ibaraki Prefectural University of Health Sciences.

MRI and ^{1}H-MRS Measurements

MRI and ^{1}H-MRS were performed on a 7.0T MRI scanner (20 cm bore, Biospec, Avance-III system; Bruker Biospin, Ettlingen, Germany) with a volume coil for transmission (86 mm i.d., Bruker Biospin) and a 2-channel phased-array cooled surface coil for reception (cryoprobe for mouse brain, Bruker Biospin), using almost the same methods as those previously reported (6). Briefly, coronal, sagittal, and axial multislice T1-weighted imaging (T1WI: multislice spin echo [SE]; repetition time [TR] / echo time [TE] = 400/9.57 msec) and coronal T2-mapping (multislice SE sequence, TR = 3000 msec, TE ranging from 20 to 100 msec in steps of 10 msec) were performed. T2 values were calculated in the white matter, thalamus, and cortex with image analysis software MRVision (MRVision, Winchester, MA). For single-voxel ^{1}H-MRS, a region of interest (ROI) was chosen predominantly in the

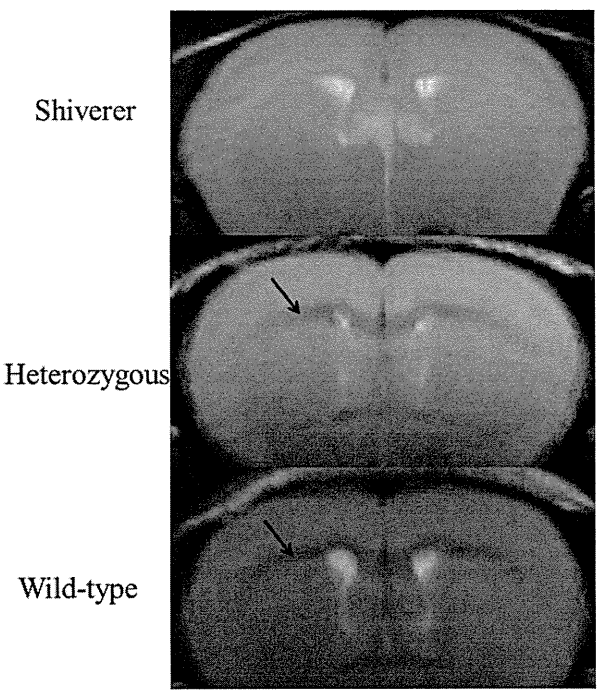

Figure 2. Coronal T2-weighted images (TE = 60 msec) of heterozygous and wild-type mice typically demonstrate a three-layered structure, ie, a low signal layer of white matter (arrows) between the cortex and caudate putamen, which was difficult to distinguish in shiverer mouse.

Table 1
T2 value of each region

	T2 value (msec, mean±SD)		
	Shiverer	Heterozygous	Wild-type
Cortex	53.3±1.8	52.3±2.0	53.1±3.3
Thalamus	53.8±1.9	51.8±2.3	51.4±2.3
White matter	55.8±1.3	48.2±1.4	48.0±1.2

***, p<0.001.

thalamus or cortex, with volumes of interest of 3.0 × 3.0 × 3.0 mm and 3.0 × 3.0 × 1.5 mm, respectively, as determined on T1WI (Fig. 1). Outer volume suppression combined with a point-resolved spectroscopy sequence was used for signal acquisition (number of repetitions = 192; TR = 4000 msec; TE = 20 msec; spectral bandwidth = 4 kHz; number of data points = 2048). ^{1}H-MRS was quantitatively analyzed using the modified water scaling method of LCModel, that is, the concentration was corrected by the T2 value of the ROI, as multiplied by R = exp (−20/T2_ROI)/0.7 (6,10). The concentrations of tNAA, creatine (Cr), Cho, myo-inositol (mIns), glutamine (Gln), and glutamate (Glu) were considered to show acceptable reliability when the LCModel showed percent of standard deviation (%SD) values of less than 20 (a smaller %SD is associated with more reliable data) (11,12).

Statistical Analysis of Metabolites

A two-way analysis of variance (ANOVA) was conducted, setting tNAA, Cr, Cho, mIns, Gln, and Glu as the dependent variables, the groups (shiverer, heterozygous, and wild-type), and the measurement sites (thalamus and cortex) as the independent variables. For each group in each measurement site, mean and SD were calculated, followed by Bonferroni's multiple comparison test on the mean difference, taking 0.05 as the significance level in testing statistical significance. The tool used for the analysis was IBM SPSS Statistics 20 (Armonk, NY).

Histological and Immunohistochemical Analyses

Two mice in each group, ie, shiverer, heterozygous, and wild-type mice, at 12W were subjected to Luxol Fast Blue (LFB) staining and immunohistochemical analysis. Coronal sections of 5 μm thickness of brain samples were prepared for these studies. The following primary antibodies were used: rat anti-Mbp antibody (1:1,000, Millipore, Bedford, MA; MAB395-IML), rabbit anti-Gfap antibody (1:500, Dako, Carpinteria, CA), rabbit anti-Olig 2 (1:100, IBL), and mouse anti-NeuN antibody (1:100, Millipore, MAB377). We defined degree of staining in the white matter, thalamus, and cortex: (−) as almost no staining, (+) as staining less than wild-type mice, (++) as staining similar to wild-type mice, (+++) as staining stronger than wild-type mice.

RESULTS

MRI Findings and T2 Value Measurement

Coronal T2 value mapping (TE = 60 msec of T2 mapping) of heterozygous and wild-type mice typically demonstrated a three-layered structure, ie, a low signal (shorter T2 value) layer of white matter between the cortex and caudate putamen, which was difficult to distinguish in shiverer mice (Fig. 2). The T2 values of the cerebral cortex, white matter, and thalamus of shiverer, heterozygous, and wild-type mice are shown in Table 1. In the white matter, the T2 values of shiverer mice were significantly longer than those of

Table 2
Concentration of metabolites (mean±SD [mM]) in the thalamus and cortex.

		NAA	Cr	Cho	mIns	Gln	Glu
Thalamus	Wt	6.96±0.51	6.95±1.04	2.01±0.09	7.12±0.70	3.50±0.27	8.86±0.41
	Htr	7.17±0.44	7.12±0.39	2.11±0.18	7.22±0.46	3.43±0.58	9.08±0.71
	Shi	6.58±0.53	6.97±0.48	1.83±0.07	7.17±0.54	3.61±0.41	8.41±0.34
Cortex	Wt	6.80±0.50	6.04±0.65	1.61±0.08	6.05±0.60	3.26±0.32	9.69±0.81
	Htr	6.45±0.48	6.04±0.32	1.57±0.09	5.91±0.54	3.19±0.42	9.28±1.07
	Shi	5.81±0.57	6.06±0.36	1.37±0.10	6.22±0.36	2.98±0.29	8.02±0.34

Mean±SD **,P<0.01 ; *,P<0.05

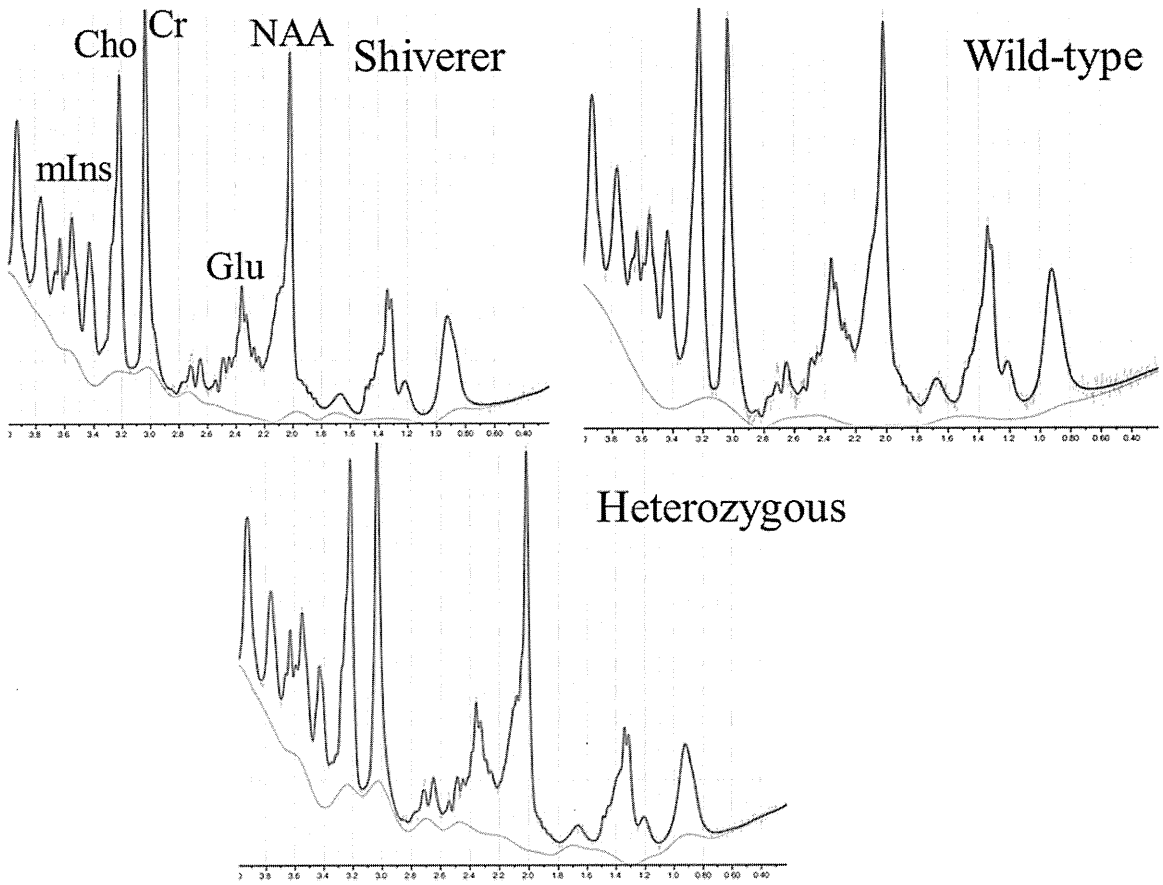

Figure 3. ^{1}H-MRS of the thalamus of shiverer mice shows reduced Cho compared with heterozygous and wild-type mice. [Color figure can be viewed in the online issue, which is available atwileyonlinelibrary.com.]

heterozygous and wild-type mice. In the cortex and thalamus, there were no differences in the T2 values among shiverer, heterozygous, and wild-type mice. Atrophic change, which may affect the concentrations of metabolite measured by water scaling methods, was not observed in either ROI.

Brain Metabolites Measured by ^{1}H-MRS

The concentrations of each metabolite in the thalamus and cortex of shiverer, heterozygous, and wild-type mice are shown in Table 2. The %SD of tNAA, Cr, Cho, mIns, and Glu in all mice were less than 5, and the mean %SD of these metabolites were less than 4 in the three groups. The %SD of Gln was less than 13, and the mean %SD was less than 10 in the three groups.

The two-way ANOVA showed significance in the main effect of the measurement sites and the groups on tNAA and Cho; significance in the main effect of the measurement sites on Cr, mIns, and Gln; and significance in the main effect and the interaction of the groups on Glu. In the thalamus, Cho was decreased in shiverer mice, compared with heterozygous and wild-type mice (Fig. 3). There were no differences in the other metabolites among the three groups. In the cortex, tNAA, Cho, and Glu were decreased in shiverer mice, compared with heterozygous and wild-type mice. There were no differences in these metabolites between heterozygous and wild-type mice; and no differences in Cr, mIns, and Gln between the three groups.

Histological and Immunohistochemical Analyses

The results of histological and immunohistochemical analyses are summarized in Table 3 and Figs. 4 and 5. LFB staining and immunostaining of Mbp, a marker for mature myelin sheaths, in shiverer mice (Fig. 4a,d) revealed sparse and weak staining in the white matter, thalamus, and cortex in comparison with heterozygous (Fig. 4b,e) and wild-type mice (Fig. 4c,f). These findings indicated hypomyelination in the

Table 3
LFB staining and immunohistochemical analyses.

	Shiverer	Heterozygous	Wild-type
LFB	- (GM,WM,Th)	++	++
Mbp	- (GM,WM,Th)	+ (GM,WM,Th)	++
GFAP	+++ (WM)	++	++
Oligo-2	+++ (WM)	++	++
NeuN	+ (GM)	++	++

GM, gray matter; WM, white matter; Th, thalamus; (-), almost no staining; (+), staining less than wild-type mice; (++), staining similar to wild-type mice; (+++), staining stronger than wild-type mice.

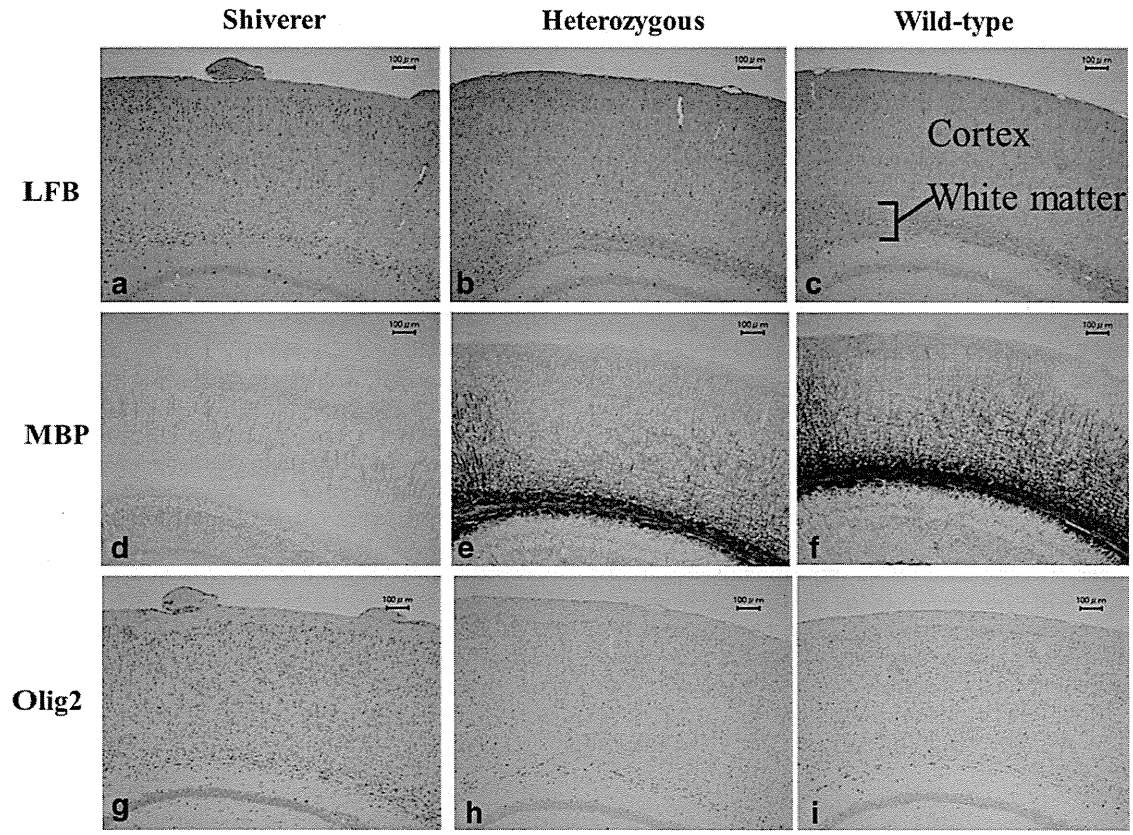

Figure 4. LFB staining and immunostaining of Mbp in shiverer mice (**a,d**) revealed sparse and weak staining in the white matter and cortex in comparison with heterozygous (**b,e**) and wild-type mice (**c,f**), indicating hypomyelination. Immunostaining of Mbp in heterozygous mice (**e**) showed slightly reduced immunoactivity in all regions, compared with wild-type mice (**f**). Olig2 immunostaining of shiverer mice (**g**) revealed increased immunoreactivity in the white matter, compared with heterozygous (**h**) and wild-type mice (**i**), showing an increased number of total oligodendrocytes (OPCs and mature oligodendrocytes). Scale bars = 100 μm.

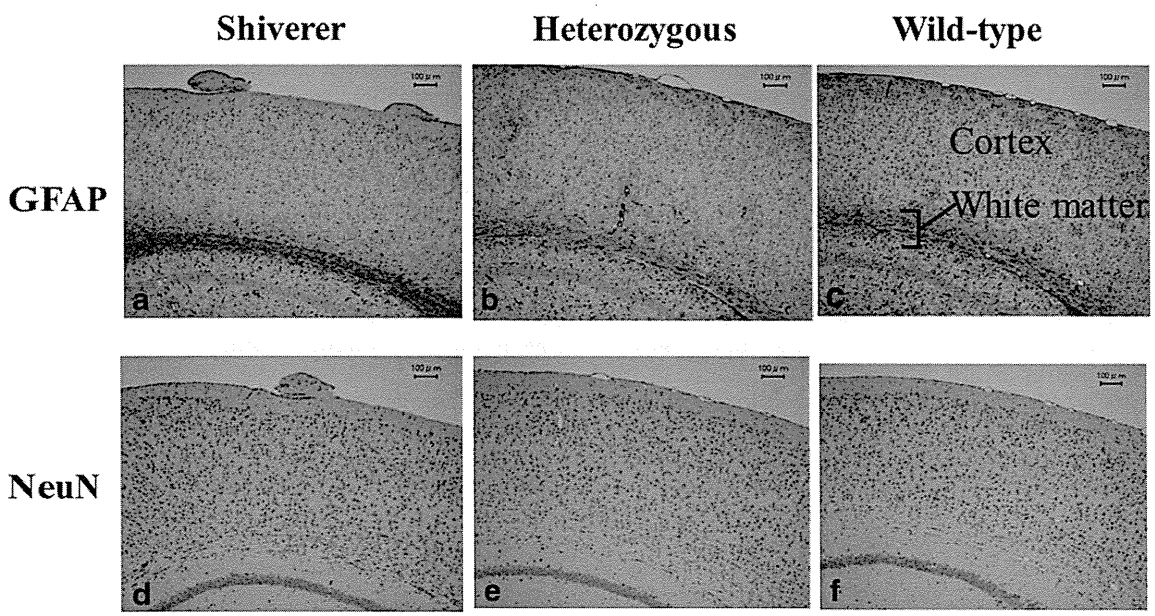

Figure 5. Gfap immunostaining of the shiverer mice (**a**) showed dense and strong staining in the white matter compared with heterozygous and wild-type mice (**b,c**), indicating astrogliosis in the white matter of shiverer mice. NeuN immunostaining of shiverer mice (**d**) revealed decreased immunoreactivity in the cortex (especially on its surface) compared with heterozygous and wild-type mice (**e,f**). Scale bars = 100 μm.

shiverer mice brains at 12W. Immunostaining of Mbp in heterozygous mice (Fig. 4e) showed slightly reduced immunoactivity in all regions, compared with wild-type mice (Fig. 4f). Gfap immunostaining, a marker for astrocytes, of the shiverer mice (Fig. 5a) showed dense and strong staining in the white matter compared with heterozygous and wild-type mice (Fig. 5b,c), indicating astrogliosis in the white matter of shiverer mice. Olig2 immunostaining, a marker for both mature and immature oligodendrocytes of shiverer mice (Fig. 4g), revealed increased immunoreactivity in the white matter, compared with heterozygous and wild-type mice (Fig. 4h,i). The number of the Olig2-positive cells in the white matter was more in shiverer mice (1460, 1220 cells/mm^2) than heterozygous (560, 620 cells/mm^2) and wild-type mice (420, 520 cells/mm^2). This indicated an increased number of total oligodendrocytes (oligodendrocyte progenitor cells [OPCs] and mature oligodendrocytes) in the white matter of shiverer mice. There were no obvious differences in Gfap and Olig2 immunostaining in the thalamus and the cortex between the three groups. NeuN immunostaining, a marker for neuronal cells of shiverer mice (Fig. 5d), revealed decreased immunoreactivity in the cortex (especially on its surface), compared with heterozygous and wild-type mice (Fig. 5e,f), but no obvious difference in the thalamus or white matter.

DISCUSSION

^{1}H-MRS in the thalamus of shiverer mice with the *mbp* mutation revealed a decrease in Cho with normal tNAA, which is distinct from in *msd* mice with the *plp1* mutation that show a decrease in Cho with an increase in tNAA (6). These findings suggest that increased tNAA is not directly related to hypomyelination. NeuN immunostaining (a marker for neuronal cells) of the thalamus in both shiverer and *msd* mice revealed no difference compared with wild-type mice; therefore, the number of neuronal cells in the thalamus seems unlikely to explain the difference in tNAA.

What is the cause of the difference in tNAA observed on ^{1}H-MRS between the two hypomyelinating strains? Mbp immunostaining indicated hypomyelination in the shiverer mice brain, as observed in the *msd* mice brain (6). Reflecting the pathology, shiverer mice exhibited longer T2 values than heterozygous and wild-type mice in the white matter, as also observed in *msd* mice brain (6). Mutant plp1 proteins in *msd* mice are abnormally folded and accumulated in the endoplasmic reticulum, resulting in the activation of an unfolded protein response that finally leads to oligodendrocyte apoptotic death before normal myelination occurs (13). In *msd* and also in another PMD mouse model, *jimpy*, massive apoptosis of oligodendrocytes appears to induce proliferation of OPCs in the white matter (14,15), leading to an increase of OPCs and the absence of mature oligodendrocytes. On the other hand, the absence of mbp protein in shiverer mice results in the failure of oligodendrocytes to form a compact myelin sheath. Unlike in *msd* and *jumpy* mice, OPCs in shiverer mice can differentiate into oligodendrocytes, and both OPCs and mature oligodendrocytes are increased in number by as much as two times (16), as shown on Olig2 immunostaining (Fig. 4g). One possible explanation for the difference in tNAA is the different patterns of oligodendrocytes in shiverer and *msd* mice.

NAA is one of the most highly abundant free amino acids in the CNS (around 10 mM in man), and it is generally considered to be an important marker of neurons and axons (8,9). NAA is either released from neurons or transported to oligodendrocytes, where it is catabolized by aspartoacylase into acetate and aspartate (17), which are used for fatty acid and steroid synthesis, and energy production, respectively. In *msd* mice, the absence or dysfunction of mature oligodendrocytes may either disable neuron-to-oligodendrocyte NAA transport or affect NAA catabolism in oligodendrocytes, leading to NAA accumulation in neurons. An elevated NAA concentration also increases NAAG biosynthesis (9), which probably results in increased tNAA on ^{1}H-MRS. On the other hand, NAA in shiverer mice may be normally transported from neurons to oligodendrocytes, and then catabolized into acetate and aspartate, leading to normal tNAA on ^{1}H-MRS. In the cortex of shiverer mice, tNAA is decreased compared with wild-type and heterozygous mice, probably reflecting the decreased number of neuronal cells in shiverer mice, as shown on NeuN immunostaining. The majority of excitatory neurons in the cerebral cortex release Glu, which is taken up from the synaptic cleft by surrounding astrocytes and metabolized into a relatively harmless compound, Gln. Therefore, Glu and Gln are considered to be markers of neurons and astrocytes, respectively. The decrease of Glu in the cortex of shiverer mice supports the theory that a decrease in tNAA reflects a decreased number of neuronal cells.

Another detectable metabolic change in shiverer mice is a reduction of Cho, which is also observed in *msd* mice (6) and patients with PMD (7). However, the degree of Cho reduction in the thalamus of shiverer mice compared with that in wild-type mice (−6.6%) is much less than that in *msd* mice (−21.8%). The Cho peak likely contains various cell membrane precursors or breakdown products such as phosphocholine, glycerophosphocholine, and phosphatidylcholine. Thus, Cho increases in association with accelerated myelination in infantile brains (18), and probably decreases in association with the severe retardation of myelination. ^{1}H-MRS in vitro demonstrated that cultured oligodendrocytes per se had a higher concentration of Cho than neurons, astrocytes, and OPCs (19,20). The different degrees of Cho reduction in the two hypomyelination strains may be explained by the pathological difference of oligodendrocytes, that is, severe hypomyelination with an increased number of oligodendrocytes in shiverer mice (16), leading to a mild reduction of Cho, and the severe hypomyelination with the absence of oligodendrocytes in *msd* mice (14), resulting in a severer reduction of Cho. Whatever the cause, the reduction of

Cho might be a marker for hypomyelinating disorders on ^{1}H-MRS.

Heterozygous mice (*shi/+*) have been reported to be clinically asymptomatic, and to exhibit normal brain MRI (21,22). They also have been shown to have normal myelin sheaths by electron microscopic studies of optic nerves, although the Mbp gene expression level is 50% of normal (21), which reasonably leads to slightly reduced immunoactivity of Mbp (Fig. 4e) compared with wild-type mice. Heterozygous mice, however, exhibit a 7% increase in visually evoked potential latency, suggesting mild optic nerve dysfunction compared with wild-type mice (23). Mildly increased Cho in thalami of heterozygous mice (+5.1%), compared with wild-type mice, might also reflect a subtle myelin dysfunction, most probably increased turnover of oligodendrocytes or myelination itself.

^{1}H-MRS showed no difference in Cr among the three groups, although increased Cr has been reported in *msd* mice (6) and patients with PMD (7). The Cr peak is composed of proton resonances from both phosphocreatine and free Cr, which are involved in energy metabolism, and are present in both neuronal and glial cells. In rats, astrocytes have Cr concentrations twice as high as those observed in neurons (19). As reactive astrogliosis is observed in the *msd* mouse brain (6), the elevated Cr was considered to result from the increased number of astrocytes. Absence of any obvious difference in Gfap immunostaining (a marker for astrocytes) in the thalamus and cortex among shiverer, heterozygous, and wild-type mice is, therefore, the likely reason for the absence of difference in Cr concentration.

Some aspects of the ^{1}H-MRS in this study require discussion. Because the white matter of mice is very thin, attempts to place the ROI in the white matter result in both inadequate signal-to-noise and contamination from the adjacent cortex and deep gray nuclei. The normal thalamus is composed of a mixture of myelinated axons and neurons; therefore, ^{1}H-MRS in shiverer mice may reflect metabolic derangements of both components. Mbp immunostaining indicated hypomyelination in both the white matter and thalamus of the shiverer brain. In addition, the number of neurons in the thalamus was almost the same in shiverer, heterozygous, and wild-type mice. These suggest that ^{1}H-MRS in the thalamus reasonably reflects the metabolic derangements associated with hypomyelination. A limitation should also be mentioned regarding the pathologic examinations in this study. Only two mice of each group were pathologically examined with qualitative evaluation. The G-ratio, the ratio between axon diameter and fiber diameter (axon diameter + myelin sheath thickness) (24), sometimes used for the detailed analysis of myelination, was not evaluated in this study.

In conclusion, this study revealed a reduction of Cho with normal tNAA level in the thalamus of the shiverer mouse (a hypomyelination mutant with the absence of *mbp*). The presence of mature oligodendrocytes in shiverer mice, which enable neuron-to-oligodendrocyte NAA transport or NAA catabolism, may result in a normal tNAA level in contradistinction to the *msd* mouse (a hypomyelination mutant with absence of *plp1*). Although tNAA seems to vary depending on the underlying pathology, reduction of Cho observed on ^{1}H-MRS might be a common marker for hypomyelinating disorders.

ACKNOWLEDGMENTS

We thank Ms. Sayaka Shibata (Molecular Imaging Center, National Institute of Radiological Sciences, Chiba, Japan) for technical support; and Dr. Masaharu Hayashi (Department of Brain Development and Neural Regeneration, Tokyo Metropolitan Institute of Medical Science, Tokyo, Japan) and Dr. Kazuhiko Sawada (Faculty of Medical and Health Sciences, Tsukuba International University, Tsuchiura, Japan) for comments on pathology.

REFERENCES

1. Nave KA. Neurological mouse mutants and the genes of myelin. J Neurosci Res 1994;38:607–612.
2. Readhead C, Hood L. The dysmyelinating mouse mutants shiverer (shi) and myelin deficient (shi^{mld}). Behav Genet 1990;20: 213–234.
3. Campagnoni AT. Molecular biology of myelin proteins from the central nervous system. J Neurochem 1988;51:1–14.
4. Takanashi J, Sugita K, Tanabe Y, et al. MR-revealed myelination in the cerebral corticospinal tract as a marker for Pelizaeus-Merzbacher disease with proteolipid protein gene duplication. AJNR Am J Neuroradiol 1999;20:1822–1828.
5. Inoue K. PLP1-related inherited dysmyelinating disorders: Pelizaeus-Merzbacher disease and spastic paraplegia type 2. Neurogenetics 2005;6:1–16.
6. Takanashi J, Saito S, Aoki I, Barkovich AJ, Ito Y, Inoue K. Increased N-acetylaspartate in model mouse of Pelizaeus-Merzbacher disease. J Magn Reson Imaging 2012;35:418–425.
7. Takanashi J, Inoue K, Tomita M, et al. Brain N-acetylaspartate is elevated in Pelizaeus-Merzbacher disease with PLP1 duplication. Neurology 2002;58:237–241.
8. Moffett JR, Namboodiri MAA. Expression of N-acetylaspartate and N-acetylaspartylglutamate in nervous system. Adv Exp Med Biol 2006;576:7–26.
9. Moffett JR, Ross B, Arun P, Madhavarao CN, Namboodiri AM. N-acetylaspartate in the CNS: from neurodiagnostics to neurobiology. Prog Neurobiol 2007;81:89–131.
10. Takanashi J, Somazawa F, Maruyama K,Terada H, Xu D, Barkovich AJ. Metabolic changes in early childhood using LCModel with corrected water scaling method. J Magn Reson Imaging 2012;35:174–180.
11. Atwood T, Robbins ME, Zhu J-M. Quantitative in vivo proton MR spectroscopic evaluation of the irradiated rat brain. J Magn Reson Imaging 2007;26:1590–1595.
12. Provencher SW. LCModel & LCMgui user's manual. http://s-provencher.com/pub/LCModel/manual/manual.pdf 2013.
13. Gow A, Southwood CM, Lazzarini RA. Disrupted proteolipid protein trafficking results in oligodendrocyte apoptosis in an animal model of Pelizaeus-Merzbacher disease. J Cell Biol 1998;140: 925–934.
14. Skoff RP. Increased proliferation of oligodendrocytes in the hypomyelinating mouse mutant-jimpy. Brain Res 1982;248:19–31.
15. Nishiyama A. Glial progenitor cells in normal and pathological states. Keio J Med 1998;47:205–208.
16. Bu J, Banki A, Wu Q, Nishiyama A. Increased NG2$^+$ glial cell proliferation and oligodendrocyte generation in the hypomyelinating mutant shiverer. Glia 2004;48:51–63.
17. Bhakoo KK, Craig TJ, Styles P. Developmental and regional distribution of aspartoacylase in rat brain tissue. J Neurochem 2001; 79:211–220.
18. Grodd W, Krageloh-Mann I, Klose U, Sauter R. Metabolic and destructive brain disorders in children: findings with localized proton MR spectroscopy. Radiology 1991;181:173–181.

19. Urenjak J, Williams SR, Gadian DG, Noble M. Proton nuclear magnetic resonance spectroscopy unambiguously identifies different neural cell types. J Neurosci 1993;13:981–989.
20. Jansen JFA, Shamblott MJ, van Zijl PCM, et al. Stem cell profiling by nuclear magnetic resonance spectroscopy. Magn Reson Med 2006;56:666–670.
21. Shine HD, Readhead C, Popko B, Hood L, Sidman RL. Morphometric analysis of normal, mutant, and transgenic CNS: correlation of myelin basic protein expression to myelinogenesis. J Neurochem 1992;58:342–349.
22. Tanaka R, Iwasaki N, Hayashi M, et al. Abnormal brain MRI signal in 18q- syndrome not due to dysmyelination. Brain Dev 2012;34:234–237.
23. Martin M, Hiltner TD, Wood JC, Fraser SE, Jacobs RE, Readhead C. Myelin deficiencies visualized in vivo: visually evoked potentials and T2-weighted magnetic resonance images of shiverer mutant and wild-type mice. J Neurosci Res 2006;84:1716–1726.
24. Chomiak T, Hu B. What is the optimal value of the g-ratio for myelinated fibers in the rat CNS? A theoretical approach. PLoS One 2009;4:e7754.